

# Multi-scale Lagrangian shock hydrodynamics on Q1/P0 finite elements: Theoretical framework and two-dimensional computations <sup>☆</sup>

G. Scovazzi <sup>a,\*</sup>, E. Love <sup>a</sup>, M.J. Shashkov <sup>b</sup>

<sup>a</sup> 1431 Computational Shock- and Multi-Physics Department, Sandia National Laboratories, P.O. Box 5800, MS 1319, Albuquerque, NM 87185-1319, USA

<sup>b</sup> Theoretical Division, Group T-7, MS B284, Los Alamos National Laboratory, Los Alamos, NM 87545, USA

Received 28 June 2007; received in revised form 28 September 2007; accepted 3 October 2007

Available online 17 October 2007

## Abstract

A new multi-scale, stabilized method for Q1/P0 finite element computations of Lagrangian shock hydrodynamics is presented. Instabilities (of hourglass type) are controlled by a stabilizing operator derived using the variational multi-scale analysis paradigm. The resulting stabilizing term takes the form of a pressure correction. With respect to broadly accepted hourglass control approaches, the novelty of the method resides in its residual-based character. The stabilizing residual has a definite physical significance, since it embeds a discrete form of the Clausius–Duhem inequality. Effectively, the proposed stabilization samples the production of entropy to counter numerical instabilities. The proposed technique is applied to materials with no shear strength (e.g., fluids), for which there exists a caloric equation of state, and extensions to the case of materials with shear strength (e.g., solids) are also envisioned. The stabilization operator is incorporated into a mid-point, predictor/multi-corrector time integration algorithm, which conserves mass, momentum and total energy. Encouraging numerical results in the context of compressible gas dynamics confirm the potential of the method.

© 2007 Elsevier B.V. All rights reserved.

**Keywords:** Lagrangian shock hydrodynamics; Variational multi-scale method; Stabilization; Hourglass instability

## 1. Introduction

In [25,24], the variational multi-scale approach was applied in finite element computations of Lagrangian shock hydrodynamics. In that case, a piecewise linear, continuous approximation in space was adopted for all the solution variables.

Given the encouraging results in [25], extensions to the case of Q1/P0 finite element are investigated in the present work. The notation Q1/P0 refers to the piecewise linear, continuous approximation of the kinematic variables (posi-

tion/displacement, velocity, acceleration), and the piecewise constant, discontinuous approximation of the thermodynamic variables (density, pressure, internal energy).

Among the requirements in developing a consistent formulation, conservation of mass, momentum and total energy are considered essential. In addition, a straightforward definition of the total energy of the system is also considered very important. In fact, most of the finite element implementations for shock hydrodynamics leverage a central difference time integrator in which velocities are staggered in time with respect to displacements/accelerations (see, e.g., [7] for a review of the state of the practice). Although very efficient in terms of storage and computational cost, such central difference implementations suffer from a cumbersome definition of the kinetic energy, which involves the product of algorithmic velocities at two different time instants. This is seen as a problem by the authors, since, by definition, the algorithmic kinetic energy is not ensured to be positive [7].

<sup>☆</sup> This research was partially funded by the DOE NNSA Advanced Scientific Computing Program and the Computer Science Research Institute at Sandia National Laboratories. Sandia is a multiprogram laboratory operated by Sandia Corporation, a Lockheed Martin Company, for the United States Department of Energy under contract DEAC04-94-AL85000.

\* Corresponding author. Tel.: +1 505 844 0707.

E-mail address: [gscovaz@sandia.gov](mailto:gscovaz@sandia.gov) (G. Scovazzi).

The present paper proposes an alternative approach, in which a mid-point type integrator is implemented by means of a conservative predictor/multi-corrector procedure. Thanks to this approach, a straightforward definition of the total energy is obtained. To the authors' best knowledge, the proposed algorithm is new in finite element hydrocode implementations, although a similar approach was originally proposed by Caramana et al. [8], in the context of mimetic finite differences. The proposed approach also shares significant similarities with the space-time integrators discussed in [25].

At the core of the algorithm is a novel, multi-scale operator which controls hourglass type instabilities. Applying the multi-scale analysis [17,18] to the base Galerkin formulation shows how instabilities can be controlled. For materials with no shear strength (e.g., fluids) the stabilization takes the form of a *pressure enrichment*, ultimately dependent on the *residual* of a rate equation for the pressure. The residual character of the stabilization preserves the consistency of the method, and, at the same time, reveals important connections between numerical instabilities and physical aspects of the problem simulated. In fact, the pressure equation residual can be interpreted as a statement of the Clausius–Duhem entropy inequality [1,31,32]. Effectively, the pressure residual *samples* and *counters* the production of entropy due to numerical instabilities. Previous work has gone in the direction of *physical hourglass control design* [3,4,23]: the present work takes an even closer look at the interplay between physical consistency and numerical instabilities of algorithms.

The proposed approach can be extended to solids with shear strength in two and three dimensions, for which the stabilizing pressure update residual is replaced by the residual of the full stress rate equation. In the present work, however, only computations in two dimensions for compressible fluids are considered. The extension to three-dimensional fluids presents some additional issues, since in that case, half of the space of hourglass modes is represented by pointwise divergence-free modes, which do not produce any residual in the rate equation for the pressure. This particular aspect poses an interesting *dilemma*: On the one hand, because the fluid is inviscid, the physics of the problem requires no shear damping, while on the other hand, the numerical discretization requires some control for divergence-free modes. In our opinion, this is not a fault of the multi-scale approach, rather, a drawback of the Q1/P0 formulation which needs to be addressed by *any* hourglass control technique. In [26], a control over the divergence-free part of the hourglass space was introduced, using a viscosity operator constructed with the fine-scale deviator of the velocity gradient, with encouraging results. We hope to report soon on this subject with extensive computations in three dimensions.

An integral part of the proposed approach is the shock-capturing operator, in the form of an artificial stress tensor, based on the symmetric part of the velocity gradient. This choice, already explored in [25], yields an *objective* stress

tensor, which proves superior to standard artificial viscosity operators, constructed with the velocity divergence. Whenever spurious *homogeneous shear* modes are generated across the shock layer, the tensor viscosity delivers much improved results, from both the accuracy and robustness standpoints. In particular, improvements with respect to [25] on the selection of the length scale in the artificial viscosity are discussed.

The rest of the exposition is organized as follows: the basic equations of Lagrangian hydrodynamics are introduced in Section 2. The variational formulation is established in Section 3, and the time integration algorithm is described in Section 4. Section 5 is devoted to the multi-scale analysis and design of the multi-scale hourglass stabilization. The shock-capturing operator is described in Section 6. Section 7 contains additional comments on the implementation of the algorithm, the integration quadratures used, and the time step CFL constraints for the method. Results of the numerical tests are analyzed in Section 8. Conclusions and future research perspectives are summarized in Section 9.

## 2. Equations of Lagrangian shock hydrodynamics

The equations of Lagrangian shock hydrodynamics govern the rate of change in position, momentum and total energy of a compressible body of fluid, as it deforms. Let  $\Omega_0$  and  $\Omega$  be open sets in  $\mathbb{R}^{n_d}$  (where  $n_d$  is the number of spatial dimensions). The *deformation*

$$\boldsymbol{\varphi} : \Omega_0 \rightarrow \Omega = \boldsymbol{\varphi}(\Omega_0), \quad (1)$$

$$\mathbf{X} \mapsto \mathbf{x} = \boldsymbol{\varphi}(\mathbf{X}, t), \quad \forall \mathbf{X} \in \Omega_0, t \geq 0, \quad (2)$$

is a *smooth*, invertible map from the original to the current configuration of the material. Here  $\mathbf{X}$  is the material coordinate, representing the initial position of an infinitesimal material particle of the body, and  $\mathbf{x}$  is the position of that particle in the current configuration (see Fig. 1).  $\Omega_0$  is the domain occupied by the body in its initial configuration, with boundary  $\Gamma_0$ .  $\boldsymbol{\varphi}$  maps  $\Omega_0$  to  $\Omega$ , the domain occupied by the body in its current configuration, with boundary  $\Gamma$ . It is also useful to define the *deformation gradient*, and the *deformation Jacobian determinant*:

$$\mathbf{F} = \nabla_{\mathbf{X}} \boldsymbol{\varphi} \quad \text{or} \quad F_{iA} = \frac{\partial \varphi_i}{\partial X_A} = \frac{\partial x_i}{\partial X_A}, \quad (3)$$

$$J = \det(\mathbf{F}). \quad (4)$$

On a domain  $\Omega$  in the current configuration, the conservative form of the equations of Lagrangian hydrodynamics, consisting of mass, momentum and energy, can be written as follows:

$$\rho J = \rho_0, \quad (5)$$

$$\rho \dot{\mathbf{v}} = \rho \mathbf{g} + \nabla_{\mathbf{x}} \cdot \boldsymbol{\sigma}, \quad (6)$$

$$\rho \dot{E} = \rho \mathbf{g} \cdot \mathbf{v} + \rho r + \nabla_{\mathbf{x}} \cdot (\boldsymbol{\sigma}^T \mathbf{v} + \mathbf{q}), \quad (7)$$

$$\dot{\mathbf{u}} = \mathbf{v}. \quad (8)$$

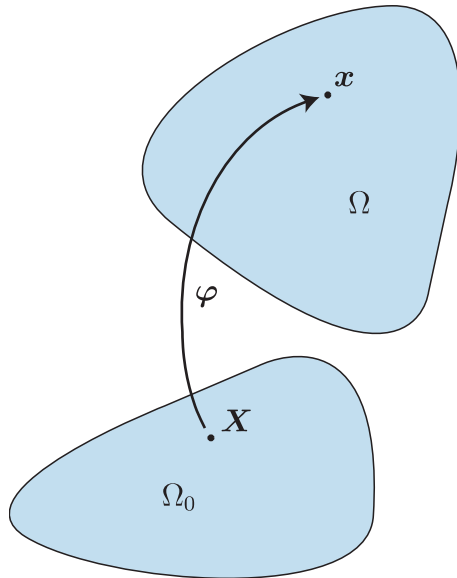


Fig. 1. Sketch of the Lagrangian map  $\varphi$ .

Here,  $\nabla_{\mathbf{x}}$  and  $\nabla_{\mathbf{x}^*}$  are the current configuration gradient and divergence operators, and  $(\dot{\cdot})$  indicates the material, or Lagrangian, time derivative.  $\mathbf{u} = \mathbf{x} - \mathbf{X}$  is the displacement vector,  $\rho_0$  is the reference (initial) density,  $\rho$  is the (current) density,  $\mathbf{v}$  is the velocity,  $\mathbf{g}$  is the body force,  $\boldsymbol{\sigma}$  is the Cauchy stress (a symmetric tensor),  $E = \epsilon + \mathbf{v} \cdot \mathbf{v}/2$  is the total energy, the sum of the internal energy  $\epsilon$  and the kinetic energy  $\mathbf{v} \cdot \mathbf{v}/2$ ,  $r$  is the energy source term, and  $\mathbf{q}$  is the heat flux.  $E, \epsilon, \mathbf{g}, r$  are measured per unit mass.

**Remarks**

- (1) Eqs. (6) and (7) are in Lagrangian *conservative* (or divergence) form. In fact, the Lagrangian rate of change of an intensive, scalar variable  $\phi$  is given by

$$\begin{aligned} \frac{d}{dt} \int_{\Omega} \rho \phi \, d\Omega &= \frac{d}{dt} \int_{\Omega} \rho_0 \phi \, d\Omega_0 = \int_{\Omega} \rho_0 \dot{\phi} \, d\Omega_0 \\ &= \int_{\Omega} \rho \dot{\phi} \, d\Omega, \end{aligned} \tag{9}$$

where (5) has been used, together with the identity  $\rho_0 \, d\Omega_0 = \rho J \, d\Omega_0 = \rho \, d\Omega$ . (10)

- (2) The kinetic energy equation, the inner product of (6) and the velocity vector field, can be subtracted from Eq. (7), yielding

$$\rho \dot{\epsilon} = \rho r + \nabla_{\mathbf{x}} \mathbf{v} : \boldsymbol{\sigma} + \nabla_{\mathbf{x}} \cdot \mathbf{q}, \tag{11}$$

where in index notation,  $\boldsymbol{\sigma}^T : \nabla_{\mathbf{x}} \mathbf{v} = \sigma_{ji} \partial_{x_i} v_j$ , and  $\nabla_{\mathbf{x}} \mathbf{v} : \boldsymbol{\sigma} = \boldsymbol{\sigma} : \nabla_{\mathbf{x}} \mathbf{v} = \boldsymbol{\sigma}^T : \nabla_{\mathbf{x}} \mathbf{v}$ , since  $\boldsymbol{\sigma}$  is symmetric. Clearly (11) is not in conservative form. However, it will be possible to use this equation in appropriate variational formulations maintaining global conservation properties (see Section 4).

The system of equations (5)–(8) has to be complemented with appropriate boundary conditions. Assuming that the boundary  $\Gamma = \partial\Omega$  is partitioned as  $\Gamma = \Gamma^g \cup \Gamma^h$ ,  $\Gamma^g \cap \Gamma^h = \emptyset$ , displacement boundary conditions are applied on  $\Gamma^g$ , the Dirichlet boundary, and traction boundary conditions are applied on  $\Gamma^h$ , the Neumann boundary. Namely,

$$\mathbf{u}|_{\Gamma^g} = \mathbf{u}_{bc}(\mathbf{x}, t), \tag{12}$$

$$\boldsymbol{\sigma} \mathbf{n}|_{\Gamma^h} = \mathbf{t}(\mathbf{x}, t). \tag{13}$$

Eqs. (5)–(8) and boundary conditions (12) and (13) completely define the evolution of the system, once appropriate initial conditions are specified.

*2.1. Constitutive laws*

The analysis presented in what follows is specific to materials with no deformation strength. In this case, the Cauchy stress  $\boldsymbol{\sigma}$  reduces to an isotropic tensor, dependent only on the thermodynamic pressure:

$$\boldsymbol{\sigma} = -p \mathbf{I}_{n_d \times n_d} \tag{14}$$

or in index notation,

$$\sigma_{ij} = -p \delta_{ij}, \tag{15}$$

with  $\delta_{ij}$  the Kronecker tensor. An equation of state of the type

$$p = \hat{p}(\rho, \epsilon), \tag{16}$$

is assumed. Equations of state of Mie-Grüneisen type are compatible with (16), namely

$$\hat{p}(\rho, \epsilon) = f_1(\rho) + f_2(\rho)\epsilon, \tag{17}$$

and apply to materials such as compressible ideal gases, co-volume gases, high explosives, and elastic–plastic solids with no strength (a situation that can be achieved when bulk stresses in the material are larger than shear stresses by orders of magnitude). For example, ideal gases satisfy (17), with  $f_1 = 0$  and  $f_2 = (\gamma - 1)\rho$ , to yield

$$\hat{p}(\rho, \epsilon) = (\gamma - 1)\rho\epsilon. \tag{18}$$

**3. Variational formulation of Lagrangian hydrodynamics**

Finite element approximations leverage a variational statement of the equations of motion. The first step in the development of a variational form for (5)–(7) (or (11)), and (8), is to define the (variational) *trial* spaces for the kinematic and thermodynamic variables, which characterize the *state* of the system. In particular,  $\mathcal{S}_\kappa$  denotes the space of admissible displacements, or more generally, the space of admissible values for the kinematic variables (displacements, velocities, accelerations). Analogously,  $\mathcal{S}_\gamma$  is the space of admissible thermodynamic states. Specific discrete definitions of  $\mathcal{S}_\kappa$  and  $\mathcal{S}_\gamma$  are given in the next section, where the discrete form of the variational equations is presented. For now, it is important to observe that the space  $\mathcal{S}_\kappa$  incorporates the set of *essential* boundary conditions

(12), that is, boundary conditions of kinematic (Dirichlet) type are imposed *strongly*. In addition, *test* spaces can be defined:  $\mathcal{V}_\kappa$  is the space of variations – compatible with (12) – for the kinematic variables, and  $\mathcal{V}_\gamma$  is the space of variations for the thermodynamic variables. Using (9) and (10), the variational problem associated with (5), (6), (11) reads:

Find  $\rho \in \mathcal{S}_\gamma$ ,  $\mathbf{v} \in \mathcal{S}_\kappa$ , and  $\epsilon \in \mathcal{S}_\gamma$ , such that,  $\forall \psi_\gamma \in \mathcal{V}_\gamma$ , and  $\forall \psi_\kappa \in \mathcal{V}_\kappa$ ,

$$0 = \int_{\Omega_0} \psi_\gamma (\rho_0 - \rho J) d\Omega_0, \quad (19)$$

$$0 = \int_{\Omega_0} \psi_\kappa \cdot (\rho_0 \dot{\mathbf{v}}) d\Omega_0 + \int_{\Omega} \nabla_x^s \psi_\kappa : \boldsymbol{\sigma} d\Omega - \int_{\Omega} \psi_\kappa \cdot (\rho \mathbf{g}) d\Omega - \int_{\Gamma^h} \psi_\kappa \cdot \mathbf{t} d\Gamma, \quad (20)$$

$$0 = \int_{\Omega_0} \psi_\gamma (\rho_0 \dot{\epsilon}) d\Omega_0 - \int_{\Omega} \psi_\gamma (\nabla_x^s \mathbf{v} : \boldsymbol{\sigma} + \nabla_x \cdot \mathbf{q} + \rho r) d\Omega, \quad (21)$$

where  $\nabla_x^s = 1/2(\nabla_x^T + \nabla_x)$  is the symmetric part of the gradient operator, and  $\nabla_x \mathbf{v} : \boldsymbol{\sigma} = \nabla_x^s \mathbf{v} : \boldsymbol{\sigma}$ , since  $\boldsymbol{\sigma}$  is symmetric. Notice that the traction (or *natural*) boundary conditions are imposed in (20) through the weak form.

#### 4. Time integration and discrete weak forms

The variational form of the Lagrangian hydrodynamics equations and its conservation properties are related to the choice of time integration algorithm. In the present work, a mid-point type integration scheme is adopted, which, in combination with an appropriate predictor/corrector solution strategy, yields an explicit iterative algorithm. The proposed formulation conserves mass, momentum and total energy, without resorting to any staggered approach in time, with striking analogies to the space-time integration presented in [25]. A similar approach is usually adopted in the context of *mimetic* or *compatible* discretizations [8,2].

##### 4.1. Test and trial spaces

In terms of the spatial discretization, the proposed approach is no different from standard Lagrangian hydrodynamic finite element methods [7,15]. Kinematic variables are approximated by piecewise linear, continuous functions (node-centered degrees-of-freedom), and all thermodynamic variables are approximated by piecewise constant, discontinuous functions (cell-centered degrees-of-freedom). Consequently, the test-space for the momentum equation consists of piecewise linear, continuous functions, while the test-space for the mass and energy equations is given by piecewise constant, discontinuous functions. The trial function spaces  $\mathcal{S}^h$  and test function spaces  $\mathcal{V}^h$  are then given by

$$\mathcal{S}_\kappa^h = \{ \psi_\kappa^h \in (C^0(\Omega))^{n_d} : \psi_\kappa^h|_{\Omega_e} \in (\mathcal{P}_1(\Omega_e))^{n_d}, \psi_\kappa^h = \mathbf{g}_{bc}(t) \text{ on } \Gamma^g \}, \quad (22)$$

$$\mathcal{V}_\kappa^h = \{ \psi_\kappa^h \in (C^0(\Omega))^{n_d} : \psi_\kappa^h|_{\Omega_e} \in (\mathcal{P}_1(\Omega_e))^{n_d}, \psi_\kappa^h = \mathbf{0} \text{ on } \Gamma^g \}, \quad (23)$$

$$\mathcal{S}_\gamma^h = \{ \psi_\gamma^h \in L^2(\Omega) : \psi_\gamma^h|_{\Omega_e} \in \mathcal{P}^0(\Omega_e) \}, \quad (24)$$

$$\mathcal{V}_\gamma^h = \mathcal{S}_\gamma^h, \quad (25)$$

where  $\mathbf{g}_{bc}(t)$  indicates the essential (Dirichlet) boundary conditions, possibly dependent on time.

##### 4.2. Variational equations

The momentum and energy balances are considered first. For the sake of simplicity, it is assumed that body forces, heat fluxes and heat sources are absent. The time step is indicated by  $\Delta t$ , and the mid-point value of a quantity  $f$  is defined as

$$f_{n+1/2} = \frac{f_n + f_{n+1}}{2}. \quad (26)$$

###### 4.2.1. Momentum balance

Find  $\mathbf{v} \in \mathcal{S}_\kappa^h$ , such that,  $\forall \psi_\kappa^h \in \mathcal{V}_\kappa^h$ ,

$$\int_{\Omega_0} \psi_\kappa^h \cdot \rho_0 (\mathbf{v}_{n+1} - \mathbf{v}_n) d\Omega_0 + \Delta t \int_{\Omega_{n+1/2}} (\nabla_x \psi_\kappa^h)_{n+1/2} : \tilde{\boldsymbol{\sigma}}_{n+1/2} d\Omega - \Delta t \int_{\Gamma_{n+1/2}^h} \psi_\kappa^h \cdot \mathbf{t}_{n+1/2} d\Gamma = 0, \quad (27)$$

where  $\nabla_x$  is the current configuration gradient operator. Notice the slight abuse of notation, since the superscript “ $h$ ”, indicating spatial discretization, should be applied to all solution variables, discrete gradient operators, and the domain geometry. This is avoided whenever possible, to favor a simpler presentation of algebraic expressions. Notice that the physical traction  $\mathbf{t}$  acts only on the Neumann boundary (i.e.,  $\mathbf{t}|_{\Gamma^g} = 0$ ), and the notation  $\tilde{\boldsymbol{\sigma}}$  indicates an algorithmic stress, whose general expression is

$$\tilde{\boldsymbol{\sigma}} = \boldsymbol{\sigma} + \boldsymbol{\sigma}_{\text{vms}} + \boldsymbol{\sigma}_{\text{art}}, \quad (28)$$

where  $\boldsymbol{\sigma}_{\text{vms}}$  is the multi-scale, residual-based stress tensor, designed to control hourglass instabilities, and  $\boldsymbol{\sigma}_{\text{art}}$  is the artificial viscosity stress tensor, designed to capture shock layers.

It is usual practice in hydrodynamic computations to *lump* the mass matrix in the momentum equation, to avoid any matrix inversions in the solution procedure. The velocity field at time  $t_n$  is interpolated as

$$\mathbf{v}_n = \sum_{B=1}^{n_{\text{np}}} N^B(\mathbf{X}) \mathbf{v}_{n;B}. \quad (29)$$

Here  $\mathbf{v}_{n;B}$  and  $N^B(\mathbf{X})$  are the  $n_d$ -dimensional vector of velocity degrees-of-freedom at  $t_n$  and the shape function, both associated with node  $B$ , and  $n_{\text{np}}$  is the number of nodes in the computational mesh. The mass lumping is achieved

applying the following approximation (no index sum is implied unless expressly stated):

$$\begin{aligned} \int_{\Omega_n} N^A(\mathbf{X})(\rho v_i)_n d\Omega &= \int_{\Omega_0} N^A(\mathbf{X})\rho_0(v_i)_n d\Omega_0 \\ &= \sum_{B=1}^{n_{np}} \left( \int_{\Omega_0} N^A(\mathbf{X})N^B(\mathbf{X})\rho_0 d\Omega_0 \right) (v_i)_{n;B} \\ &\approx \sum_{B=1}^{n_{np}} \left( \int_{\Omega_0} N^A(\mathbf{X})\delta^{AB}\rho_0 d\Omega_0 \right) (v_i)_{n;B} \\ &= \mathcal{M}_L^A(v_i)_{n;A}, \end{aligned} \quad (30)$$

where  $v_i$  and  $v_i$  are the  $i$ th components of  $\mathbf{v}$  and  $\mathbf{v}$ , respectively,  $A = 1, 2, \dots, n_{np}$ ,  $\delta^{AB}$  is the Kronecker symbol, and

$$\mathcal{M}_L^A = \int_{\Omega_0} N^A(\mathbf{X})\rho_0 d\Omega_0 \quad (31)$$

is the mass associated to node  $A$  in the global numbering. Defining

$$[\mathbf{M}_L] = [\text{diag}\{\{\mathcal{M}_L^A, \mathcal{M}_L^A, \mathcal{M}_L^A\}^T\}], \quad (32)$$

$$\mathbf{F}_{n+1/2} = \{\mathbf{F}_{n+1/2;A}\}, \quad (33)$$

$$\begin{aligned} \mathbf{F}_{n+1/2;A} &= \int_{\Omega_{n+1/2}} \tilde{\boldsymbol{\sigma}}_{n+1/2}(\nabla_x N^A)_{n+1/2} d\Omega \\ &\quad - \int_{\Gamma_{n+1/2}} N^A \tilde{\mathbf{t}}_{n+1/2} d\Gamma, \end{aligned} \quad (34)$$

where  $[\mathbf{M}_L]$  is a diagonal  $[(n_d \times n_{np}) \times (n_d \times n_{np})]$ -matrix and  $\mathbf{F}_{n+1/2}$  is a  $(n_d \times n_{np})$ -vector, Eq. (27) reduces to

$$[\mathbf{M}_L](\mathbf{v}_{n+1} - \mathbf{v}_n) + \Delta t \mathbf{F}_{n+1/2} = \mathbf{0}. \quad (35)$$

#### 4.2.2. Energy balance

Integrating in time (21), yields:

Find  $\epsilon \in \mathcal{S}_\gamma^h$ , such that,  $\forall \psi_\gamma^h \in \mathcal{V}^h$ ,

$$\int_{\Omega_0} \psi_\gamma^h \rho_0 (\epsilon_{n+1} - \epsilon_n) d\Omega_0 - \Delta t \int_{\Omega_{n+1/2}} \psi_\gamma^h (\nabla_x \mathbf{v})_{n+1/2} : \tilde{\boldsymbol{\sigma}}_{n+1/2} d\Omega = 0. \quad (36)$$

Recalling that  $\psi_\gamma$ ,  $\epsilon$ , and  $\rho$  are constant over each element, one can introduce the following definitions:

$$[\mathbf{M}_{el}] = [\text{diag}\{\mathbf{M}_{el}\}], \quad (37)$$

$$\mathbf{M}_{el} = \{\mathcal{M}_e\}, \quad (38)$$

$$\mathcal{M}_e = \int_{\Omega_{0;e}} \rho_0 d\Omega_0. \quad (39)$$

$$\mathbf{W}_{n+1/2} = \{\mathbf{W}_{n+1/2;e}\}, \quad (40)$$

$$\mathbf{W}_{n+1/2;e} = \left\{ - \int_{\Omega_{n+1/2;e}} (\nabla_x \mathbf{v})_{n+1/2} : \tilde{\boldsymbol{\sigma}}_{n+1/2} d\Omega \right\}, \quad (41)$$

where  $\Omega_{n+1/2;e}$  is the element domain at time  $t_{n+1/2}$ ,  $\mathbf{M}_{el}$  and  $\mathbf{W}_{n+1/2}$  are  $n_{el}$ -dimensional vectors, and  $n_{el}$  is the number of elements in the computational list. Then, Eq. (36) reduces to

$$[\mathbf{M}_{el}](\epsilon_{n+1} - \epsilon_n) + \Delta t \mathbf{W}_{n+1/2} = \mathbf{0}. \quad (42)$$

where  $\epsilon_n$  and  $\epsilon_{n+1}$  are the vectors of cell-centered degrees-of-freedom for the internal energy  $\epsilon$  at time  $t_n$  and  $t_{n+1}$ , respectively.

#### 4.2.3. Mass balance

The mass conservation equation (19) can be slightly rearranged to yield:

Find  $\rho \in \mathcal{S}_\gamma^h$ , such that,  $\forall \psi_\gamma^h \in \mathcal{V}^h$ ,

$$\int_{\Omega_0} \psi_\gamma^h \rho_0 d\Omega_0 = \int_{\Omega_0} \psi_\gamma^h \rho J d\Omega_0 = \int_{\Omega} \psi_\gamma^h \rho d\Omega. \quad (43)$$

Integrating the previous equation element-by-element at time  $t_{n+1}$ , yields

$$\mathbf{M}_{el} = [\mathbf{V}_{n+1}] \boldsymbol{\rho}_{n+1}, \quad (44)$$

where

$$\boldsymbol{\rho}_{n+1} = \{\rho_{n+1;e}\}, \quad (45)$$

$$[\mathbf{V}_{n+1}] = [\text{diag}\{\mathbf{V}_{n+1}\}], \quad (46)$$

$$\mathbf{V}_{n+1} = \{\mathbf{V}_{n+1;e}\}, \quad (47)$$

$$\mathbf{V}_{n+1;e} = \int_{\Omega_{0;e}} J_{n+1} d\Omega_0 = \text{meas}(\Omega_{n+1;e}). \quad (48)$$

#### 4.2.4. Displacement equations

In order to evaluate (44), the mesh geometry has to be computed at time  $t_{n+1}$ . This is possible by means of the time-discretization of the rate equations for the position field  $\mathbf{x}$ , which yields a set of ordinary differential equations for the vector of node locations, namely

$$\dot{\mathbf{x}}_{n+1} - \dot{\mathbf{x}}_n - \Delta t \mathbf{v}_{n+1/2} = \mathbf{0}. \quad (49)$$

#### 4.2.5. Equation of state

The equation of state can be applied at each time step to obtain the pressure (or, in general, the stress field),

$$\boldsymbol{\sigma}_{n+1} = -p_{n+1} \mathbf{I} = -\hat{p}(\rho_{n+1}, \epsilon_{n+1}) \mathbf{I}. \quad (50)$$

Expressing (50) in terms of the cell-centered degrees-of-freedom, one obtains

$$\boldsymbol{\rho}_{n+1} = \hat{\mathbf{p}}(\boldsymbol{\rho}_{n+1}, \epsilon_{n+1}), \quad (51)$$

where

$$\boldsymbol{\rho}_{n+1} = \{\rho_{n+1;e}\}, \quad (52)$$

$$\hat{\mathbf{p}}(\boldsymbol{\rho}_{n+1}, \epsilon_{n+1}) = \{\hat{p}(\rho_{n+1;e}, \epsilon_{n+1;e})\}. \quad (53)$$

### 4.3. Global conservation properties

Eqs. (43) and (44) are statements of global and local conservation of mass, respectively. It is also evident from Eq. (27) or (35) that the proposed algorithm conserves the total momentum of the system. Proving conservation of total energy is somewhat less obvious, and, for this purpose, Eqs. (27) and (36) are used. Conservation statements

are usually proven in the case of homogenous Neumann boundary conditions, for which the test and trial function spaces for the velocities coincide (i.e.,  $\mathcal{S}_\kappa^h = \mathcal{V}_\kappa^h$ ). Evaluating the sum over all the nodes of (27), with  $\psi_\kappa^h = \mathbf{v}_{n+1/2}$ , the kinetic energy balance for the system is obtained

$$\begin{aligned} & \frac{1}{2} \int_{\Omega_{n+1}} \rho_{n+1} (\mathbf{v} \cdot \mathbf{v})_{n+1} d\Omega - \frac{1}{2} \int_{\Omega_n} \rho_n (\mathbf{v} \cdot \mathbf{v})_n d\Omega \\ &= -\Delta t \int_{\Omega_{n+1/2}} (\nabla_x \mathbf{v})_{n+1/2} : \tilde{\boldsymbol{\sigma}}_{n+1/2} d\Omega, \end{aligned} \quad (54)$$

The previous equation is derived using the following identity:

$$\begin{aligned} & \int_{\Omega_0} \rho_0 \mathbf{v}_{n+1/2} \cdot (\mathbf{v}_{n+1} - \mathbf{v}_n) d\Omega_0 \\ &= \frac{1}{2} \int_{\Omega_0} \rho_0 ((\mathbf{v} \cdot \mathbf{v})_{n+1} - (\mathbf{v} \cdot \mathbf{v})_n) d\Omega_0 \\ &= \frac{1}{2} \int_{\Omega_{n+1}} \rho_{n+1} (\mathbf{v} \cdot \mathbf{v})_{n+1} d\Omega - \frac{1}{2} \int_{\Omega_n} \rho_n (\mathbf{v} \cdot \mathbf{v})_n d\Omega. \end{aligned} \quad (55)$$

Testing (36) with a shape function equal to unity over the entire domain (i.e.,  $\psi_\gamma^h|_{\Omega_0} = 1$ ) yields

$$\begin{aligned} & \int_{\Omega_{n+1}} (\rho \epsilon)_{n+1} d\Omega - \int_{\Omega_n} (\rho \epsilon)_n d\Omega = \int_{\Omega_0} \rho_0 (\epsilon_{n+1} - \epsilon_n) d\Omega_0 \\ &= \Delta t \int_{\Omega_{n+1/2}} (\nabla_x \mathbf{v})_{n+1/2} : \tilde{\boldsymbol{\sigma}}_{n+1/2} d\Omega. \end{aligned} \quad (56)$$

By summing (54) and (56), and noticing that their right hand sides are equal and opposite, one can derive the following conservation statement for the total energy between time steps  $n$  and  $n+1$ :

$$\begin{aligned} & \int_{\Omega_{n+1}} \rho_{n+1} \left( \frac{1}{2} (\mathbf{v} \cdot \mathbf{v})_{n+1} + \epsilon_{n+1} \right) d\Omega \\ &= \int_{\Omega_n} \rho_n \left( \frac{1}{2} (\mathbf{v} \cdot \mathbf{v})_n + \epsilon_n \right) d\Omega. \end{aligned} \quad (57)$$

The previous derivations can be repeated in the case when mass lumping is applied. Using (35), an analogue of (54) can be derived, namely,

$$\frac{1}{2} \mathbf{v}_{n+1}^T [\mathbf{M}_L] \mathbf{v}_{n+1} - \frac{1}{2} \mathbf{v}_n^T [\mathbf{M}_L] \mathbf{v}_n = -\mathbf{v}_{n+1/2}^T \mathbf{F}_{n+1/2}. \quad (58)$$

Using the vector notation, (56) can be recast as (42) multiplied by  $\mathbf{1}$ , a  $n_{\text{el}}$ -dimensional vector whose entries are all unity, that is,

$$\mathbf{M}_{\text{el}}^T (\boldsymbol{\epsilon}_{n+1} - \boldsymbol{\epsilon}_n) = -\Delta t \mathbf{1}^T \mathbf{W}_{n+1/2}. \quad (59)$$

Finally, realizing that, by definition,

$$\mathbf{v}_{n+1/2}^T \mathbf{F}_{n+1/2} = -\mathbf{1}^T \mathbf{W}_{n+1/2}, \quad (60)$$

a statement of conservation of total energy analogous to (57) can be expressed as

$$\frac{1}{2} \mathbf{v}_{n+1}^T [\mathbf{M}_L] \mathbf{v}_{n+1} + \mathbf{M}_{\text{el}}^T \boldsymbol{\epsilon}_{n+1} = \frac{1}{2} \mathbf{v}_n^T [\mathbf{M}_L] \mathbf{v}_n + \mathbf{M}_{\text{el}}^T \boldsymbol{\epsilon}_n. \quad (61)$$

## Remarks

- (1) Under appropriate boundary conditions, total angular momentum is also conserved. This is a direct consequence of the symmetry of the stress tensor and the use of a mid-point time integrator [29].
- (2) The total energy conservation statement (57) is a direct consequence of the cancellation of the right hand sides of (54) and (56), which are equal and opposite. This fact is used to derive artificial viscosity and variational multi-scale stabilization operators which preserve total energy in the system. In fact, to ensure conservation, it is sufficient that the discrete expression for the overall  $\tilde{\boldsymbol{\sigma}}$  term remains the same in the momentum and energy equations.

### 4.4. A predictor/multi-corrector approach

The algorithm developed so far requires the inversion of a matrix, since the force and work terms are computed at the mid-point in time, and necessitate knowledge of the solution at time  $t_{n+1}$ . However, a fully explicit algorithm can be recovered by resorting to a predictor/multi-corrector approach. This section is devoted to this purpose.

A number of preliminary definitions are needed. The state of system at time  $t = t_n$  is defined by means of the vector  $\mathbf{Y}_n = [\mathbf{x}_n^T, \mathbf{v}_n^T, \boldsymbol{\rho}_n^T, \boldsymbol{\epsilon}_n^T, \mathbf{p}_n^T]^T$ .  $\mathbf{F}_{n+1/2}^{(i)}$  indicates the evaluation of  $\mathbf{F}_{n+1/2}$  using the state  $\mathbf{Y}$  at iterate  $(i)$ . The definition of the iterate of the work vector  $\mathbf{W}_{n+1/2}$  is somewhat different

$$\mathbf{W}_{n+1/2}^{(i,j)} = \{ \mathbf{W}_{n+1/2;e}^{(i,j)} \}, \quad (62)$$

$$\mathbf{W}_{n+1/2;e}^{(i,j)} = \left\{ \int_{\Omega_{n+1/2;e}^{(i)}} ((\nabla_x)^{(i)} \mathbf{v}_{n+1/2}^{(j)}) : \tilde{\boldsymbol{\sigma}}_{n+1/2}^{(i)} d\Omega \right\}. \quad (63)$$

Here  $(\nabla_x)^{(i)}$  and  $\mathbf{v}_{n+1/2}^{(j)}$  indicate the (current configuration) gradient operator and the velocity field at  $t = t_{n+1/2}$  and iterate  $i$  and  $j$ , respectively. This notation is needed to understand how conservation is enforced *at each iteration* of the predictor/multi-corrector procedure.

As it can be appreciated in Table 1, the proposed approach consists of a velocity update, followed, in the order, by internal energy, position, volume, density and pressure (or, more generally, stress) updates.

**Remark (conservation of total energy).** The proposed predictor/multi-corrector approach maintains all the conservation properties of the base mid-point algorithm it is derived from. The crucial step in the design of the algorithm is to recognize that the work vector  $\mathbf{W}_{n+1/2}^{(i,i+1)}$  in Table 1 has to be computed holding the geometry and all the terms in the integral (63) at iterate  $(i)$ , with the exception of the velocity  $\mathbf{v}_{n+1/2}$ , which is evaluated using the new iterate  $(i+1)$ , available after the momentum equation is integrated in time. Using arguments virtually identical to the ones presented in Section 4.3, it is easy to

Table 1  
Outline of the predictor–multi-corrector algorithm

---

Retrieve loop parameters: $n_{\text{step}}, i_{\text{max}}$
Initialize all variables with initial conditions
Form $[\mathbf{M}_L]$ and $\mathbf{M}_{\text{el}}$
<b>For</b> $n = 0, \dots, n_{\text{step}}$ ( <i>Time-step loop begins</i> )
Set $\Delta t$ (respecting the CFL condition)
Predictor: $\mathbf{Y}_{n+1}^{(0)} = \mathbf{Y}_n$
<b>For</b> $i = 0, \dots, i_{\text{max}} - 1$ ( <i>Multi-corrector loop begins</i> )
Assembly: $\mathbf{F}_{n+1/2}^{(i)}$
Velocity update: $\mathbf{v}_{n+1}^{(i+1)} = \mathbf{v}_n - \Delta t [\mathbf{M}_L]^{-1} \mathbf{F}_{n+1/2}^{(i)}$
Assembly: $\mathbf{W}_{n+1/2}^{(i+1)}$
Internal energy update: $\epsilon_{n+1}^{(i+1)} = \epsilon_n - \Delta t [\mathbf{M}_{\text{el}}]^{-1} \mathbf{W}_{n+1/2}^{(i+1)}$
Position update: $\mathbf{x}_{n+1}^{(i+1)} = \mathbf{x}_n + \Delta t \mathbf{v}_{n+1/2}^{(i+1)}$
Volume update: $\mathbf{V}_{n+1}^{(i+1)} = \mathbf{V}(\mathbf{x}_{n+1}^{(i+1)})$
Density update: $\rho_{n+1}^{(i+1)} = [\mathbf{V}_{n+1}^{(i+1)}]^{-1} \mathbf{M}_{\text{el}}$
Equation of state update: $\mathbf{p}_{n+1}^{(i+1)} = \hat{\mathbf{p}}(\rho_{n+1}^{(i+1)}, \epsilon_{n+1}^{(i+1)})$
<b>End</b> ( <i>Multi-corrector loop ends</i> )
Time update: $\mathbf{Y}_{n+1} = \mathbf{Y}_{n+1}^{(i_{\text{max}})}$
<b>End</b> ( <i>Time-step loop ends</i> )
<b>Exit</b>

---

Notice that all matrices are diagonal, so that all inverse operations are just vector divisions. Three iterations of the predictor/multi-corrector were used in the computations. Recall also that  $\mathbf{Y}_n = [\mathbf{x}_n^T, \mathbf{v}_n^T, \rho_n^T, \epsilon_n^T, \mathbf{p}_n^T]^T$ .

realize that, indeed, *each iterate* of the predictor/multi-corrector conserves total energy, namely

$$\frac{1}{2} (\mathbf{v}_{n+1}^{(i+1)})^T [\mathbf{M}_L] \mathbf{v}_{n+1}^{(i+1)} + \mathbf{M}_{\text{el}}^T \epsilon_{n+1}^{(i+1)} = \frac{1}{2} \mathbf{v}_n^T [\mathbf{M}_L] \mathbf{v}_n + \mathbf{M}_{\text{el}}^T \epsilon_n, \quad (64)$$

since the following cancellation takes place

$$(\mathbf{v}_{n+1/2}^{(i+1)})^T \mathbf{F}_{n+1/2}^{(i)} = -\mathbf{1}^T \mathbf{W}_{n+1/2}^{(i+1)}. \quad (65)$$

The numerical evidence in Fig. 6a, in the context of blast-type flows, show that the proposed method indeed conserves total energy within machine precision.

## 5. A multi-scale, residual-based hourglass control

The present section develops an analysis of the Lagrangian shock hydrodynamics equations, using an approach similar to [17,18,20]. The final goal is to *stabilize hourglass instabilities while retaining the global conservation properties* of the underlying discretization. A *minimalistic* approach is pursued, in the sense that the simplest and most efficient expression for the hourglass control term is sought. In the case of materials with no shear strength, the proposed strategy leads to a stabilization term in the form of a *pressure enrichment*, very easy to incorporate in state-of-the-practice hydrocodes.

### 5.1. Variational multi-scale analysis

Assume that the exact solution for the state  $\mathbf{Y} = [\mathbf{x}^T, \mathbf{v}^T, \rho, \epsilon, p]^T \in \mathcal{S}$  of the system can be decomposed as  $\mathbf{Y} = \mathbf{Y}^h + \mathbf{Y}^l$ .  $\mathbf{Y}^h \in \mathcal{S}^h$  is the *mesh-* or *coarse-scale* solution, represented by the discrete approximation space  $\mathcal{S}^h$  used to characterize the solution on the computational

grid.  $\mathbf{Y}^l \in \mathcal{S}^l$  is the *subgrid-* or *fine-scale* solution, the component of the solution which cannot be represented on the computational mesh. Obviously,  $\mathcal{S} = \mathcal{S}^h \oplus \mathcal{S}^l$ .

In (27)–(36), the explicit notations  $\psi_\kappa^h$  and  $\psi_\gamma^h$  were used to indicate that the equations for the *exact* state of the system are tested on the discrete test function space  $\mathcal{V}^h$ . The superscript “*h*” for the components of the solution  $\mathbf{Y}^h$  was omitted in most of the derivations in Section 4, since in that case there was no risk of confusion. In the discussion that follows, however, it is important to precisely account for the fine- and coarse-scale spaces. Hence

$$\mathbf{v} = \mathbf{v}^h + \mathbf{v}', \quad (66)$$

$$\rho_0 = \rho_0^h + \rho_0', \quad (67)$$

$$\rho = \rho^h + \rho', \quad (68)$$

$$\boldsymbol{\sigma} = \boldsymbol{\sigma}^h + \boldsymbol{\sigma}', \quad (69)$$

$$\epsilon = \epsilon^h + \epsilon'. \quad (70)$$

Using the previous decomposition, (20) and (21) reduce to

$$\int_{\Omega_0} \psi_\kappa^h \cdot (\rho_0^h + \rho_0') (\dot{\mathbf{v}}^h + \dot{\mathbf{v}}') d\Omega_0 + \int_{\Omega} (\nabla_x^s \psi_\kappa^h) : (\boldsymbol{\sigma}^h + \boldsymbol{\sigma}') d\Omega = 0, \quad (71)$$

$$\int_{\Omega_0} \psi_\gamma^h (\rho_0^h + \rho_0') (\dot{\epsilon}^h + \dot{\epsilon}') d\Omega_0 - \int_{\Omega} \psi_\gamma^h (\nabla_x^s (\mathbf{v}^h + \mathbf{v}')) : (\boldsymbol{\sigma}^h + \boldsymbol{\sigma}') d\Omega = 0, \quad (72)$$

where in order to simplify the analysis, homogenous Dirichlet boundary conditions are imposed for the velocity. *No approximation* has been made so far, and the initial geometry of the computational grid, as well as the displacement field are assumed to be known *exactly*. At this point, it becomes useful to decompose the stress  $\boldsymbol{\sigma}$  as follows:

$$\boldsymbol{\sigma} = -p\mathbf{I} + \text{dev } \boldsymbol{\sigma}, \quad (73)$$

$$p = -\frac{\text{tr } \boldsymbol{\sigma}}{3} = -\frac{1}{3} \sum_{k=1}^{n_d} \sigma_{kk}, \quad (74)$$

$$\text{dev } \boldsymbol{\sigma} = \boldsymbol{\sigma} - \frac{\text{tr } \boldsymbol{\sigma}}{3} \mathbf{I} = \boldsymbol{\sigma} + p\mathbf{I}. \quad (75)$$

An analogous decomposition holds for  $\boldsymbol{\sigma}^h$  and  $\boldsymbol{\sigma}'$ , and the generic symmetric gradient of a vector  $\mathbf{w}$ :

$$\nabla_x^s \mathbf{w} = (\nabla_x^s \cdot \mathbf{w}) \mathbf{I} + \text{dev}(\nabla_x^s \mathbf{w}). \quad (76)$$

Therefore, the stress integrals in (71) and (72) can be recast in terms of the following expressions:

$$\int_{\Omega} (\nabla_x^s \psi_\kappa^h) : \boldsymbol{\sigma}^* d\Omega = - \int_{\Omega} (\nabla_x \cdot \psi_\kappa^h) : p^* d\Omega + \int_{\Omega} \text{dev}(\nabla_x^s \cdot \psi_\kappa^h) : \text{dev } \boldsymbol{\sigma}^* d\Omega, \quad (77)$$

$$\int_{\Omega} \psi_{\gamma}^h \nabla_x^s(\mathbf{v}^{\diamond}) : \boldsymbol{\sigma}^{\bullet} d\Omega = - \int_{\Omega} \psi_{\gamma}^h (\nabla_x \cdot \mathbf{v}^{\diamond}) : p^{\bullet} d\Omega + \int_{\Omega} \psi_{\gamma}^h \text{dev}(\nabla_x^s \mathbf{v}^{\diamond}) : \text{dev} \boldsymbol{\sigma}^{\bullet} d\Omega, \quad (78)$$

where  $\boldsymbol{\sigma}^{\bullet} = \boldsymbol{\sigma}^h$  or  $\boldsymbol{\sigma}'$ ,  $p^{\bullet} = p^h$  or  $p'$ , and  $\mathbf{v}^{\diamond} = \mathbf{v}^h$  or  $\mathbf{v}'$ . Some additional assumptions are now needed to derive a simple stabilization operator.

### Assumptions I (coarse-scale equations).

- (i) Fine-scale terms are considered *small* with respect to coarse-scale terms. Therefore, products of fine-scale terms are neglected, being higher-order corrections.
- (ii) Fine-scale components of the node positions and mesh geometry are considered negligible.
- (iii)  $\rho'_0$  is considered negligible, since  $\rho_0$  is a *datum* of the problem.
- (iv) Time derivatives of the fine-scales are neglected. This *quasi-static* approximation is equivalent to assuming that the fine scales adjust instantaneously to complement the coarse-scales. Some authors [11] have been arguing in favor of tracking in time the subgrid-scale component in the solution. However, this would involve the additional computational cost of storing and integrating in time the fine-scale component of the state variables. In the current work, this additional cost is avoided.
- (v) The following integral is neglected:

$$\int_{\Omega} \psi_{\gamma}^h p^h \nabla_x \cdot \mathbf{v}' d\Omega = \sum_{e=1}^{n_{el}} \left( \psi_{\gamma;e}^h p_e^h \int_{\Omega_e} \nabla_x \cdot \mathbf{v}' d\Omega \right), \quad (79)$$

where the subscript  $e$  indicates the element values of the piecewise constant, discontinuous interpolation for  $\psi_{\gamma}^h$  and  $p^h$ . There are two important reasons to neglect this term. First of all, the typical velocity instabilities arising in the base Galerkin formulation are hourglass modes, whose divergence integrates to zero over each element. If an hourglass mode has to be counterbalanced, the corrective field  $\mathbf{v}'$  must lie in the space of hourglass modes, and its divergence must integrate to zero over each element. Therefore, assuming that (79) is negligible or vanishes is equivalent to posing the correct constraint on the fine-scale velocity space. Another important reason not to include (79) is that its discretization would yield a non-conservative formulation. Because a number of non-linear, higher-order terms have been removed from the original equations, global conservation of total energy is not ensured *a priori*, but has to be checked and enforced *a posteriori*.

- (vi) In order to obtain a conservative method, the term

$$\int_{\Omega} \psi_{\gamma}^h \text{dev}(\nabla_x^s \mathbf{v}') : \text{dev} \boldsymbol{\sigma}^h d\Omega \quad (80)$$

is also neglected. In the case of a fluid, this assumption is not needed, since  $\text{dev} \boldsymbol{\sigma}^h$  vanishes exactly.

With the previous assumptions, (71) and (72) reduce to:

$$0 = \int_{\Omega_0} \boldsymbol{\psi}_{\kappa}^h \cdot \rho_0^h \mathbf{v}^h d\Omega_0 - \int_{\Omega} (\nabla_x \cdot \boldsymbol{\psi}_{\kappa})^h p^h d\Omega + \int_{\Omega} \text{dev}(\nabla_x^s \boldsymbol{\psi}_{\kappa})^h : \text{dev} \boldsymbol{\sigma}^h d\Omega - \int_{\Omega} (\nabla_x \cdot \boldsymbol{\psi}_{\kappa})^h p' d\Omega + \int_{\Omega} \text{dev}(\nabla_x^s \boldsymbol{\psi}_{\kappa})^h : \text{dev} \boldsymbol{\sigma}' d\Omega, \quad (81)$$

$$0 = \int_{\Omega_0} \psi_{\gamma}^h \rho_0^h \boldsymbol{\epsilon}^h d\Omega_0 + \int_{\Omega} \psi_{\gamma}^h (\nabla_x \cdot \mathbf{v})^h p^h d\Omega - \int_{\Omega} \psi_{\gamma}^h \text{dev}(\nabla_x^s \mathbf{v})^h : \text{dev} \boldsymbol{\sigma}^h d\Omega + \int_{\Omega} \psi_{\gamma}^h (\nabla_x \cdot \mathbf{v})^h p' d\Omega - \int_{\Omega} \psi_{\gamma}^h \text{dev}(\nabla_x^s \mathbf{v})^h : \text{dev} \boldsymbol{\sigma}' d\Omega. \quad (82)$$

### Assumptions II (fine-scale representation).

- (vii) The constitutive law of the material is assumed to have the form [14]

$$\dot{\boldsymbol{\sigma}} = \hat{\boldsymbol{\sigma}}(\boldsymbol{\sigma}, \nabla_x \mathbf{v}), \quad (83)$$

where the structure of  $\hat{\boldsymbol{\sigma}}$  is such that objectivity of the stress update procedure is ensured. Then, testing the variational formulation on the fine-scale space  $\mathcal{V}'$ , and applying a typical multi-scale approximation to the subgrid-scale Green's function operator [25,24], the subgrid-scale stress  $\boldsymbol{\sigma}$  can be expressed with the *ansatz*:

$$\boldsymbol{\sigma}' = -\tau \text{Res}_{\sigma}^h, \quad (84)$$

$$\text{Res}_{\sigma}^h = (\mathbf{LIN}(\text{Res}_{\sigma}))^h, \quad (85)$$

$$\text{Res}_{\sigma} = \dot{\boldsymbol{\sigma}} - \hat{\boldsymbol{\sigma}}(\boldsymbol{\sigma}, \nabla_x \mathbf{v}). \quad (86)$$

where  $\mathbf{LIN}$  is a linearization operator and  $\tau$  is an appropriate scaling term to be defined subsequently. As in many error estimation techniques, it is assumed that the error  $\boldsymbol{\sigma}'$  is dependent on the numerical residual of constitutive equation,  $\text{Res}_{\sigma}^h$ .

The multi-scale approach pursued so far is very general, and may be exploited to derive stabilization techniques in the case of materials with very general constitutive laws, including solids. In the next section, materials with no shear strength are considered.

### 5.2. The case of materials with no shear strength

In the case of materials which do not possess shear strength, the terms  $\text{dev} \boldsymbol{\sigma}$ ,  $\text{dev} \boldsymbol{\sigma}^h$ , and  $\text{dev} \boldsymbol{\sigma}'$  vanish, and (81), (82) simplify to

$$\int_{\Omega_0} \boldsymbol{\psi}_{\kappa}^h \cdot \rho_0^h \mathbf{v}^h d\Omega_0 - \int_{\Omega} (\nabla_x \cdot \boldsymbol{\psi}_{\kappa})^h (p^h + p') d\Omega = 0, \quad (87)$$

$$\int_{\Omega_0} \psi_{\gamma}^h \rho_0^h \boldsymbol{\epsilon}^h d\Omega_0 + \int_{\Omega} \psi_{\gamma}^h (\nabla_x \cdot \mathbf{v})^h (p^h + p') d\Omega = 0. \quad (88)$$

### Remarks

- (1) The additional stabilization term is a pressure correction term.
- (2) The proposed approach maintains global conservation properties. In fact, the conservation statements (57), (61), and (64) hold with the substitution  $\bar{\sigma} = -(p^h + p')\mathbf{I}$ .

It now remains to find an expression for the subgrid-scale pressure  $p'$ . Using the assumption of smallness of the fine-scales, a Taylor expansion can be applied to the equation of state (16), namely

$$p' = p - p^h \approx \mathbf{LIN}(p - p^h) = (\partial_\rho \hat{p})^h \rho' + (\partial_\epsilon \hat{p})^h \epsilon'. \quad (89)$$

The linearization in (89) and the structure of the residuals for the mass conservation and internal energy equations can be exploited to yield

$$p' = -\tau((\partial_\rho \hat{p})^h \text{Res}_\rho^h + (\partial_\epsilon \hat{p})^h \text{Res}_\epsilon^h), \quad (90)$$

where

$$\text{Res}_\rho^h = (\text{Res}_\rho)^h, \quad (91)$$

$$\text{Res}_\rho = \dot{\rho} + \rho \nabla_x \cdot \mathbf{v}, \quad (92)$$

$$\text{Res}_\epsilon^h = (\text{Res}_\epsilon)^h, \quad (93)$$

$$\text{Res}_\epsilon = \dot{\epsilon} + \frac{p}{\rho} \nabla_x \cdot \mathbf{v}. \quad (94)$$

The residual  $\text{Res}_\rho$  is actually the mass balance, written in the current configuration, namely

$$0 = J^{-1} \dot{\rho}_0 = J^{-1}(\rho J) = \dot{\rho} + \rho(J^{-1} \dot{J}) = \dot{\rho} + \rho \nabla_x \cdot \mathbf{v}, \quad (95)$$

and  $\tau$  is an appropriate scaling term to be defined subsequently. As previously pointed out, it is consistent with many error estimation techniques to assume that the error  $\rho' = \rho - \rho^h$  in the density is a function of the mass conservation residual  $\text{Res}_\rho^h$ . A similar argument can be applied to the fine-scale internal energy  $\epsilon'$ . Thus, the subgrid-scale pressure can be expressed as

$$\begin{aligned} p' &= -\tau(\partial_\rho \hat{p} \text{Res}_\rho + \partial_\epsilon \hat{p} \text{Res}_\epsilon)^h \\ &= -\tau \left( \partial_\rho \hat{p} (\dot{\rho} + \rho \nabla_x \cdot \mathbf{v}) + \partial_\epsilon \hat{p} \left( \dot{\epsilon} + \frac{p}{\rho} \nabla_x \cdot \mathbf{v} \right) \right)^h \\ &= -\tau \left( \dot{\rho} + \rho \left( \partial_\rho \hat{p} + \frac{p}{\rho^2} \partial_\epsilon \hat{p} \right) \nabla_x \cdot \mathbf{v} \right)^h. \end{aligned} \quad (96)$$

To further simplify the previous expression, some thermodynamic identities are needed. The first and second law of thermodynamics combined yield the Gibbs identity [12],

$$\Theta d\eta = d\epsilon - \frac{p}{\rho^2} d\rho, \quad (97)$$

with  $\eta$  the entropy per unit mass, and  $\Theta$  the absolute temperature. Hence

$$\frac{p}{\rho^2} = \frac{\partial \epsilon}{\partial \rho} \Big|_\eta. \quad (98)$$

It is easy then to derive

$$\begin{aligned} p' &= -\tau \left( \dot{\rho} + \rho \left( \partial_\rho \hat{p} + \partial_\epsilon \hat{p} \frac{\partial \epsilon}{\partial \rho} \Big|_\eta \right) \nabla_x \cdot \mathbf{v} \right)^h \\ &= -\tau \left( \dot{\rho} + \rho \frac{\partial p}{\partial \rho} \Big|_\eta \nabla_x \cdot \mathbf{v} \right)^h = -\tau (\dot{\rho} + \rho c_s^2 \nabla_x \cdot \mathbf{v})^h \\ &= -\tau \text{Res}_p^h, \end{aligned} \quad (99)$$

where

$$\text{Res}_p = \dot{\rho} + \rho c_s^2 \nabla_x \cdot \mathbf{v}, \quad (100)$$

and  $c_s$  is the (isentropic) speed of sound in the medium. Denoting with  $h_e$  the element characteristic length scale, the value of  $\tau$  is defined as

$$\tau = c_\tau \frac{\Delta t}{2\text{CFL}} = \frac{c_\tau}{2} \frac{\Delta t}{\max_{1 \leq e \leq n_{\text{el}}} \left( \frac{c_s \Delta t}{h_e} \right)} = \frac{c_\tau}{2} \min_{1 \leq e \leq n_{\text{el}}} \left( \frac{h_e}{c_s} \right), \quad (101)$$

where  $c_\tau = 7.0$  (values in the range [5.0, 15.0] were found appropriate). The definition in (101) is analogous to the one in [25,24], and prevents the dramatic reduction of  $\tau$  when the time step is small. The expression for the multi-scale stabilization tensor is then

$$\boldsymbol{\sigma}_{\text{vms}} = -p' \mathbf{I} = \tau \text{Res}_p^h \mathbf{I}. \quad (102)$$

In the case of the proposed mid-point algorithm for time integration, (102) can be recast as

$$\boldsymbol{\sigma}_{\text{vms}} = \frac{\tau}{\Delta t} (p_{n+1}^h - p_n^h + \Delta t (\rho c_s^2)_{n+1/2}^h (\nabla_x \cdot \mathbf{v})_{n+1/2}^h) \mathbf{I}. \quad (103)$$

### Remarks

- (1) For a general material, the final expression for  $\boldsymbol{\sigma}_{\text{vms}}$  is more complicated than (102), since it involves also the deviator of the tensor  $\boldsymbol{\sigma}'$ . Specific expressions depend on the structure of the constitutive laws.
- (2) It is important to understand that in the case of fluids, fully integrating the pressure stress terms in the base Galerkin formulation does not prevent hour-glass modes. This is a consequence of the fact that the pressure is approximated with piecewise constants, and factors out of the force integral. Therefore, some additional stabilization mechanism must be provided.
- (3) In order to have a non-vanishing multi-scale stabilization term, expression (103) cannot be integrated with a single-point quadrature at the centroid of quadrilateral or hexahedral elements, where the divergence of the velocity vanishes even if spurious

hourglass modes are present. In fact, (103) must be evaluated with multi-point quadratures or equivalent difference formulas. The result summarized in (102), (103) applies to a very general class of materials, since the only assumption made is the existence of the equation of state (16).

### 5.2.1. A rational thermodynamic interpretation

The structure of the *pressure residual*  $\text{Res}_p$  is related to the Clausius–Duhem inequality for an adiabatic process of a non-dissipative material. To prove this point, the approach of *rational thermodynamics* [1,31,32] is adopted. The energy balance equation can be arranged as

$$\rho\Theta\dot{\eta} = -\nabla_x \cdot \mathbf{q} + \rho r + \mathcal{D}_{\text{int}}, \quad (104)$$

where

$$\mathcal{D}_{\text{int}} \stackrel{\text{def}}{=} \rho\Theta\dot{\eta} - \rho\dot{\epsilon} - p\nabla_x \cdot \mathbf{v}. \quad (105)$$

The Clausius–Duhem inequality [32] requires that  $\mathcal{D}_{\text{int}} \geq 0$ . Using mass conservation,  $\nabla_x \cdot \mathbf{v} = -\dot{\rho}/\rho$  and

$$\rho\mathcal{D}_{\text{int}} = p\dot{\rho} + \rho^2\Theta\dot{\eta} - \rho^2\dot{\epsilon} \geq 0. \quad (106)$$

Assume there exists a *caloric equation of state* [12], that is, a function  $\tilde{\epsilon}(\rho, \eta)$  (convex with respect to  $\rho^{-1}$  and  $\eta$ ) such that  $\epsilon = \tilde{\epsilon}(\rho, \eta)$ . Substituting this into (106) yields

$$\rho\mathcal{D}_{\text{int}} = (p - \rho^2\partial_\rho\tilde{\epsilon})\dot{\rho} + \rho^2(\Theta - \partial_\eta\tilde{\epsilon})\dot{\eta} \geq 0, \quad (107)$$

which is required to hold for all admissible thermodynamic processes. By the Coleman–Noll energy principle [1], this implies that

$$p = \rho^2\partial_\rho\tilde{\epsilon}(\rho, \eta) \quad \text{and} \quad \Theta = \partial_\eta\tilde{\epsilon}(\rho, \eta). \quad (108)$$

Thus  $\mathcal{D}_{\text{int}} = 0$ , and (104) reduces to

$$\rho\Theta\dot{\eta} = -\nabla_x \cdot \mathbf{q} + \rho r. \quad (109)$$

The only sources of entropy production are thermal diffusion and external heat sources. This is a well known result for *non-dissipative* materials [9,32]: A process is *adiabatic* ( $-\nabla_x \cdot \mathbf{q} + \rho r = 0$ ) if and only if it is *isentropic* ( $\dot{\eta} = 0$ ). The previous developments imply the existence of a pressure function

$$p \stackrel{\text{def}}{=} \tilde{p}(\rho, \eta) = \rho^2\partial_\rho\tilde{\epsilon}(\rho, \eta). \quad (110)$$

Define by

$$c_s \stackrel{\text{def}}{=} \sqrt{\partial_\rho\tilde{p}(\rho, \eta)}, \quad (111)$$

the *isentropic* speed of sound in the material. The time derivative of the pressure function results in

$$\dot{p} = c_s^2\dot{\rho} + \partial_\eta\tilde{p}(\rho, \eta)\dot{\eta}. \quad (112)$$

Again, using conservation of mass  $\dot{\rho} = -\rho\nabla_x \cdot \mathbf{v}$  this may be written as

$$\dot{p} + \rho c_s^2\nabla_x \cdot \mathbf{v} = \partial_\eta\tilde{p}(\rho, \eta)\dot{\eta}. \quad (113)$$

Assuming an adiabatic process this reduces to

$$\dot{p} + \rho c_s^2\nabla_x \cdot \mathbf{v} = \text{Res}_p = 0, \quad (114)$$

the pressure residual.

### Remark.

- (1) In practice  $\text{Res}_p^h$  is a measure of the *entropy production* due to the numerical discretization. In regions of smooth flow,  $\text{Res}_p^h$  should vanish, but because of numerical instabilities, *numerical entropy* can be generated.
- (2) The previous analysis for perfect materials also shows that the assumption of smallness of the fine-scales implies the concept of isentropic flow.
- (3) When shock waves are present in the material, the analysis in the present section does not apply. From a physical point of view, a shock wave is an infinitely thin layer in which the flow does not behave as a perfect material, due to internal dissipation mechanisms. From a numerical point of view, a shock-capturing operator typically smears the discontinuity over a few cells of the computational grid. Shock-capturing operators usually have the form of an artificial dissipation, and introduce in the material an irreversible internal mechanism.

### 5.2.2. Multi-scale stabilization revisited as hourglass control

To understand that the proposed pressure enrichment acts as an hourglass control, let us decompose the divergence of a vector  $\mathbf{w}^h$  into its average value over an element and the fluctuation with respect to the average. Namely

$$\nabla_x^h \cdot \mathbf{w}^h = \overline{\nabla_x^h \cdot \mathbf{w}^h} + \widetilde{\nabla_x^h \cdot \mathbf{w}^h}, \quad (115)$$

$$\begin{aligned} \overline{\nabla_x^h \cdot \mathbf{w}^h} &= \frac{1}{\text{meas}(\Omega_e)} \int_{\Omega_e} \nabla_x^h \cdot \mathbf{w}^h \, d\Omega \\ &= \frac{1}{\text{meas}(\Omega_e)} \int_{\Gamma_e} \mathbf{w}^h \cdot \mathbf{n} \, d\Gamma. \end{aligned} \quad (116)$$

By definition,  $\overline{\nabla_x^h \cdot \mathbf{w}^h}$  and  $\widetilde{\nabla_x^h \cdot \mathbf{w}^h}$  are orthogonal in the  $L^2$  sense. Consider the structure of the stabilization term developed in the previous section. The expressions (87) and (88) can be rearranged as

$$\begin{aligned} \int_{\Omega_e} (\nabla_x^h \cdot \boldsymbol{\psi}_\kappa^h) p' \, d\Omega &= - \int_{\Omega_e} (\nabla_x^h \cdot \boldsymbol{\psi}_\kappa^h) \tau (\dot{p}^h + (\rho c_s^2)^h \nabla_x^h \cdot \mathbf{v}^h) \, d\Omega \\ &= - \int_{\Omega_e} (\nabla_x^h \cdot \boldsymbol{\psi}_\kappa^h) \tau \left( \dot{p}^h + (\rho c_s^2)^h \overline{\nabla_x^h \cdot \mathbf{v}^h} + \widetilde{\nabla_x^h \cdot \mathbf{v}^h} \right) \, d\Omega \\ &= - \int_{\Omega_e} (\nabla_x^h \cdot \boldsymbol{\psi}_\kappa^h) \tau \left( \dot{p}^h + (\rho c_s^2)^h \overline{\nabla_x^h \cdot \mathbf{v}^h} \right) \, d\Omega \\ &\quad - \tau (\rho c_s^2)^h \int_{\Omega_e} (\nabla_x^h \cdot \boldsymbol{\psi}_\kappa^h) \left( \widetilde{\nabla_x^h \cdot \mathbf{v}^h} \right) \, d\Omega \\ &= - \tau \left( \dot{p}^h + \rho c_s^2 \overline{\nabla_x^h \cdot \mathbf{v}^h} \right) \int_{\Omega_e} (\nabla_x^h \cdot \boldsymbol{\psi}_\kappa^h) \, d\Omega + \text{HG}_{1,e}, \end{aligned} \quad (117)$$

$$\int_{\Omega_e} (\nabla_{\mathbf{x}}^h \cdot \mathbf{v}^h) p' d\Omega = -\tau \left( \dot{p}^h + (\rho c_s^2)^h \overline{\nabla_{\mathbf{x}}^h \cdot \mathbf{v}^h} \right)_e \overline{\nabla_{\mathbf{x}}^h \cdot \mathbf{v}^h} \text{meas}(\Omega_e) + \text{HG}_{2;e}, \quad (118)$$

with

$$\text{HG}_{1;e} = -\tau \int_{\Omega_e} (\rho c_s^2)^h \left( \widetilde{\nabla_{\mathbf{x}}^h \cdot \psi_{\kappa}^h} \right) \left( \widetilde{\nabla_{\mathbf{x}}^h \cdot \mathbf{v}^h} \right) d\Omega, \quad (119)$$

$$\text{HG}_{2;e} = -\tau \int_{\Omega_e} (\rho c_s^2)^h \left( \widetilde{\nabla_{\mathbf{x}}^h \cdot \mathbf{v}^h} \right)^2 d\Omega. \quad (120)$$

To provide an interpretation of (117), (118), it is important to realize that, for the proposed second-order in time algorithm,

$$\begin{aligned} \left( \dot{p}^h + (\rho c_s^2)^h \overline{\nabla_{\mathbf{x}}^h \cdot \mathbf{v}^h} \right)_e &= (\dot{p}^h - (c_s^2)^h \dot{p}^h)_e \\ &\approx \Delta t (p_{n+1}^h - p_n^h) \\ &\quad - (c_s^2)_{n+1/2}^h (\rho_{n+1}^h - \rho_n^h)_e \\ &= O(\Delta t^2). \end{aligned} \quad (121)$$

When hourglass modes arise, the expression in (121) tends to be much smaller than the terms  $\text{HG}_{1;e}$  and  $\text{HG}_{2;e}$ , which represent the discretization of a divergence – divergence dissipative operator acting on the hourglass modes.

#### Remarks

- (1) In regions where a shock is present and the artificial viscosity operator is active, (121) may not hold.
- (2) Notice that  $\text{HG}_{1;e}$  and  $\text{HG}_{2;e}$  scale with the square of the speed of sound and the density of the material, similarly to many hourglass control viscosities [5].
- (3) In order for the hourglass control to work, the  $\text{HG}_{1;e}$  and  $\text{HG}_{2;e}$  terms must be evaluated at locations where the discrete divergence operator is non-vanishing. Therefore, the velocity divergence in (103) requires either full integration or equivalent, less expensive, finite difference formulas. Instead, the thermodynamic variables require only one evaluation per element.
- (4) As already mentioned in the introduction, the extension to three dimensions is non-trivial, since, in that case, half of the space of hourglass modes is represented by pointwise divergence-free modes, which do not produce any residual in the rate equation for the pressure. A possible solution to this problem is presented in [26], in which an artificial viscosity based on the fluctuation of the deviator of the velocity gradient (75) is used to control divergence-free hourglass modes. Encouraging (although preliminary) results have been obtained with this approach.

The previous observations can also be used to define an alternative class of hourglass operators. The basic idea is to define a time interpolation for  $(\rho c_s^2)^h$ , so that, element-by-

element,  $(\dot{p}^h + \rho^h c_s^2 \overline{\nabla_{\mathbf{x}}^h \cdot \mathbf{v}^h})_e$  vanishes exactly. This can be done with a *secant approximation* of  $\rho c_s^2$ , enforcing explicitly

$$(\rho c_s^2)_{n+1/2}^h \stackrel{\text{def}}{=} \frac{p_{n+1}^h - p_n^h}{\Delta t \overline{\nabla_{\mathbf{x}}^h \cdot \mathbf{v}^h}}. \quad (122)$$

If this is the case, the stabilization term reduces to:

$$\int_{\Omega_e} (\nabla_{\mathbf{x}}^h \cdot \psi_{\kappa}^h) p' d\Omega = \text{HG}_{1;e}, \quad (123)$$

$$\int_{\Omega_e} (\nabla_{\mathbf{x}}^h \cdot \mathbf{v}^h) p' d\Omega = \text{HG}_{2;e}. \quad (124)$$

This alternative class of stabilization operators is clearly augmenting the original variational formulation by means of a *purely* dissipative operator. A different choice of the scaling for  $\tau$  is also possible in this case, namely,

$$\tilde{\tau}_e = \tilde{\tau}|_{\Omega_e} = \tau \frac{h_e}{c_s \Delta t}, \quad (125)$$

where  $\tau$  is defined as in (101), and this time  $c_{\tau} = 3.0$  (values in the range [1.0, 7.0] were found appropriate). The notation  $h_e$  represents a characteristic element mesh length, for which many possible definitions can be used. If  $h_e = (\text{meas}(\Omega_e))^{1/n_d}$  is chosen, then the stabilization term introduced would scale like the viscous part of the Flanagan–Belytschko hourglass control [13,33,14,5].

#### 6. Artificial viscosity and discontinuity capturing operator

The discontinuity capturing operator is implemented as follows:

$$\boldsymbol{\sigma}_{\text{art}} = \begin{cases} \rho v_{\text{art}} \nabla_{\mathbf{x}}^s \mathbf{v}, & \text{if } \nabla_{\mathbf{x}} \cdot \mathbf{v} < 0, \\ \mathbf{0}_{n_d \times n_d}, & \text{otherwise.} \end{cases} \quad (126)$$

#### Remarks.

- (1) The use of the symmetric gradient in the definition of  $\boldsymbol{\sigma}_{\text{art}}$  ensures, at the continuum level, objectivity of the artificial viscosity operator.
- (2) The definition (126) is more effective in damping artificial pure shear motion, with respect to the more common definition [7]

$$\boldsymbol{\sigma}_{\text{art}} = -(\rho v_{\text{art}} \nabla_{\mathbf{x}} \cdot \mathbf{v}) \mathbf{I}. \quad (127)$$

Artificially produced homogeneous shear motion can have disruptive consequences on shock hydrodynamics computations of fluids, since it is not resisted by hourglass controls (of any type), nor the discretized physical stress.

Several choices of the artificial viscosity parameter  $v_{\text{art}}$  are possible. Among the most commonly used,

$$v_{\text{Kur}} = \left( c_{\text{Kur}_2} \frac{\gamma - 1}{4} v_{\text{VNR}} + \sqrt{\left( c_{\text{Kur}_2} \frac{\gamma - 1}{4} v_{\text{VNR}} \right)^2 + c_{\text{Kur}_1}^2 c_s^2} \right) h_{\text{art}}, \quad (128)$$

with  $c_{\text{Kur}_1} = c_{\text{Kur}_2} = 1$ ,  $\gamma$  the isentropic constant in the gas, and

$$v_{\text{VNR}} = |\nabla_{\mathbf{x}} \cdot \mathbf{v}| h_{\text{art}}. \quad (129)$$

Another possible choice is

$$v_{L+\text{VNR}} = c_1 c_s h_{\text{art}} + c_2 |\nabla_{\mathbf{x}} \cdot \mathbf{v}| h_{\text{art}}^2, \quad (130)$$

which was used in the computations of Section 8, with constants  $c_1 = 0.5$  and  $c_2 = 1.2$ . The expression for the so-called Kuropatenko viscosity  $v_{\text{Kur}}$  [21] holds only for an ideal gas, but can be generalized for any material. The expression for  $v_{L+\text{VNR}}$  is already general enough to include all materials satisfying (15) and (16). The length-scale  $h_{\text{art}}$  needs to be defined according to one main requirement: It should *stably* sample a mesh length along the normal to the shock front. This means that, for a given mesh,  $h_{\text{art}}$  should not vary abruptly for small changes in the direction of the shock normal. An effective definition was found to be

$$h_{\text{art}} = \frac{2}{\sqrt{\mathbf{n}_{\text{sh}}^T (\mathbf{F}_{\square} \mathbf{F}_{\square}^T)^{-1} \mathbf{n}_{\text{sh}}}}, \quad (131)$$

$$\mathbf{F}_{\square} = \frac{\partial \mathbf{x}}{\partial \xi}, \quad (132)$$

where  $\mathbf{n}_{\text{sh}}$  is a unit vector in the direction normal to the shock front, and  $\mathbf{F}_{\square}$  the gradient of the mapping from the parent domain to the element in the current configuration. In practice,  $(\mathbf{F}_{\square} \mathbf{F}_{\square}^T)$  measures the *stretch* in the direction given by  $\mathbf{n}_{\text{sh}}$ . A plot of the envelope of  $h_{\text{art}}$  as the shock normal angle spans the interval  $[0, 360]$ -degrees is presented in Fig. 2, for various quadrilateral elements. This definition

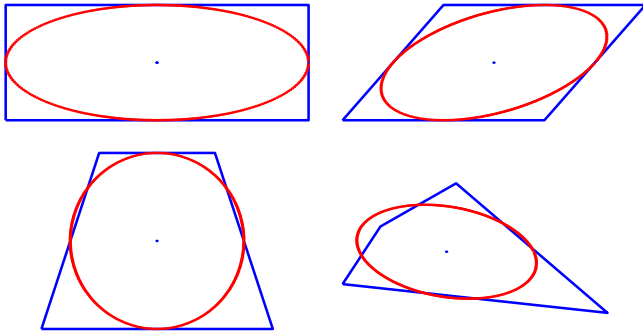


Fig. 2. Sketch of the length-scale  $h_{\text{art}}$  as a function of the direction of  $\mathbf{n}_{\text{sh}}$ . The plots show the envelope of  $h_{\text{art}}$  as the angle that  $\mathbf{n}_{\text{sh}}$  forms with the  $x_1$ -axis varies from  $0^\circ$  to  $360^\circ$ . Notice the smooth transition of the length-scale near the corners of the elements.

is analogous to the one adopted in [19]. An effective approximation to  $\mathbf{n}_{\text{sh}}$  is given by

$$\mathbf{n}_{\text{sh}} = \frac{\nabla_{\mathbf{x}} f_{\mathbf{b}}}{\|\nabla_{\mathbf{x}} f_{\mathbf{b}}\|}, \quad (133)$$

$$f_{\mathbf{b}} = \frac{\|\mathbf{v}\|_{l^2}}{\max_{1 \leq e \leq n_{\text{el}}} (\|\mathbf{v}\|_{l^2})} + 10^{-3} \frac{\hat{\rho}}{\max_{1 \leq e \leq n_{\text{el}}} (\hat{\rho})}, \quad (134)$$

where  $\|\mathbf{v}\|_{l^2} = \sqrt{\mathbf{v} \cdot \mathbf{v}}$  is the velocity magnitude, and  $\hat{\rho}$  is the nodal projection of the density, namely

$$\hat{\rho} = \sum_{A=1}^{n_{\text{np}}} \hat{\rho}_A N_A(\mathbf{X}), \quad (135)$$

$$\hat{\rho}_A = \frac{\mathbf{A}_{e=1}^{n_{\text{el}}} \int_{\Omega_e} N_A \rho d\Omega}{\mathbf{A}_{e=1}^{n_{\text{el}}} \int_{\Omega_e} N_A d\Omega} = \frac{\mathbf{A}_{e=1}^{n_{\text{el}}} (\rho_e \int_{\Omega_e} N_A d\Omega)}{\mathbf{A}_{e=1}^{n_{\text{el}}} \int_{\Omega_e} N_A d\Omega}, \quad (136)$$

with  $\mathbf{A}$  the assembly operator [16,5].

## Remarks

- (1) The definitions (133) and (134) are meant to use primarily the gradient of the velocity magnitude as a measure of the shock normal. There are a number of cases – such as implosions with radial or spherical symmetry – in which the simple use of the gradient of the velocity norm may produce noisy results in the region preceding the shock location. This is why  $f_{\mathbf{b}}$  rather than  $\|\mathbf{v}\|_{l^2}$  is introduced. The use of the gradient of the projected nodal density is reminiscent of [30].
- (2) The tensor  $\sigma_{\text{art}}$  just defined is evaluated at the mid-point in time, together with the other terms contributing to the nodal forces. Collocation at the mid-point in time ensures *incremental objectivity* of the tensor  $\sigma_{\text{art}}$  [28].

## 7. General considerations on implementation

### 7.1. Numerical quadratures

First and foremost, as already noted, the divergence of the velocity in the pressure residual  $\text{Res}_p^h$  vanishes at the centroid of quadrilateral or hexahedral elements. Therefore, four/eight-point quadratures must be used to compute the stabilization term. Notice that all other terms in the pressure residual are constant over each of the elements, and do not need multi-point evaluation. The hour-glass control for divergence-free shear modes in three dimensions also requires multi-point quadratures.

Second, when the shock-capturing operator is active, non-linear coupling effects may take place between the artificial viscosity and the multi-scale stabilization operator, as already mentioned. The optimal choice is to integrate *both* the artificial viscosity and the multi-scale operator with the same quadrature rule. With this approach, incidentally, the computational cost for the

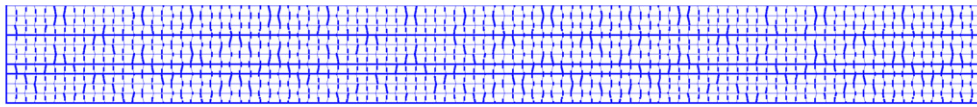
multi-scale operator is negligible with respect to the cost of the artificial viscosity, since the divergence of the velocity is needed by both. Some examples of the effects of single-point and multi-point integration for the viscosity are presented in Section 8.3.

To understand why superior results are obtained when the multi-scale and artificial viscosity operators share the same quadrature rule, one needs to recall that where the artificial dissipation is active, the multi-scale approach is not strictly applicable. A single-point evaluation of the artificial viscosity is equivalent to enforcing that the value of the artificial viscosity is constant over the entire element. Especially in the case of rapid transients, this may be a coarse approximation. Indeed, on a particular element of

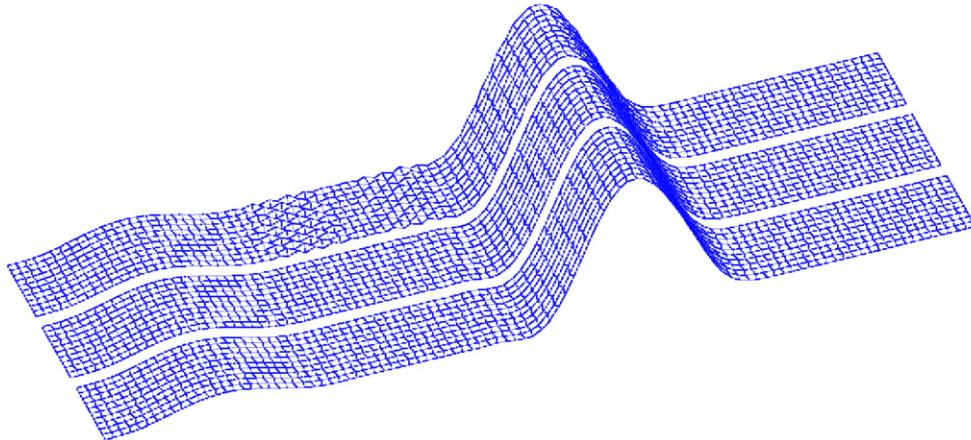
the mesh, the artificial viscosity may be active only in just a few of the quadrature points. Single-point integration redistributes the effect of the artificial viscosity over the entire element, generating a spurious pressure residual at the quadrature points where there should be no artificial dissipation. In the end, the multi-scale approach, which leverages a local evaluation of the residual, may be affected by the incorrect evaluation of the artificial dissipation.

In terms of quadrature rules, the details of the implementation can be then summarized as follows:

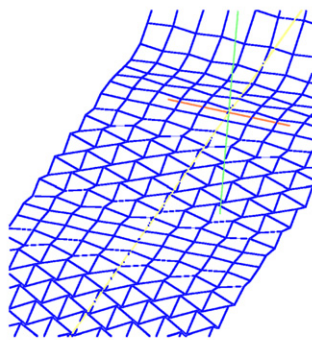
- (1) The integral of the physical stress term  $\sigma$  is evaluated with a single-point quadrature at the centroid of the element.



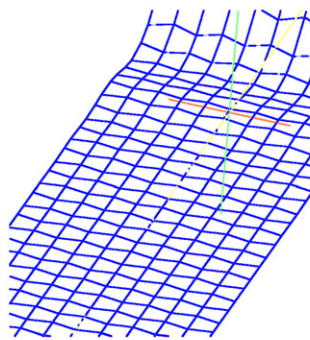
(a) Initial mesh with nodes positioned according to a typical hourglass pattern.



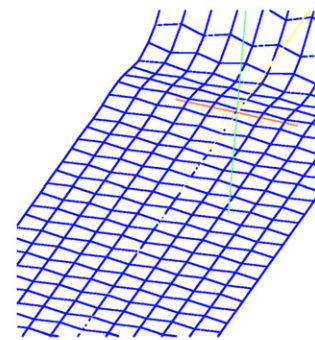
(b) Elevation plot of the  $x_1$ -component of the velocity. Top: No hourglass control. Center: VMS-I. Bottom: FB.



(c) No hourglass control, zoomed view from Figure 3(b).



(d) VMS-I hourglass control, zoomed view from Figure 3(b).



(e) FB hourglass control, zoomed view from Figure 3(b).

Fig. 3. Acoustic pulse test on an hourglass-shaped mesh. Notice the fluctuations in the velocity at the foot of the left- and right-moving acoustic waves, in the case of no hourglass control (c). These instabilities are absent when the VMS-I (d) or FB (e) stabilization is applied.

- (2) The multi-scale residual-based stabilization operator is computed with multi-point quadratures.
- (3) Unless otherwise specified, it should be implicitly assumed that the artificial viscosity operator is integrated with full quadrature.

7.2. Hourglass stabilization and artificial viscosity parameters

Most of the numerical results are obtained using the multi-scale operator as defined in (103). This method is denoted by VMS-I, and the choice  $c_\tau = 7$  is made to evaluate expression (101) (a range of recommended values could be [5.0, 15.0]). In addition, some computations using the approach of (119) and (120) are performed. This method is denoted by VMS-II, and the choice  $c_\tau = 3$  is made to evaluate expression (125) (a range of recommended values could be [1.0, 5.0]).

In order to compare the proposed multi-scale method with existing approaches, a viscous-type hourglass control *à la* Flanagan–Belytschko [5,13,14,33] is also used: This method is referred to as FB. Unless otherwise specified,

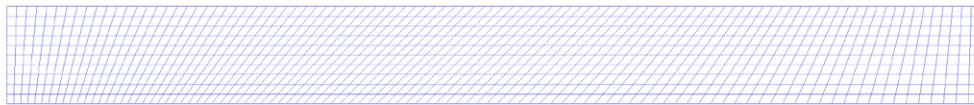
the constant parameter is chosen to be  $c_{FB} = 0.15$ . Typical recommended values [14] span the interval [0.05, 0.15]. The choice of making the hourglass control as dissipative as possible within the recommended range has the purpose of maximizing robustness. The hourglass control proposed in [13] incorporates viscous and stiffness operators, while in the simulations presented herein only the viscous part is retained. It is the opinion of the authors that incorporating artificial stiffness in the hourglass control is questionable in the case of a fluid. In any case, the results for compressible flow computations using a stiffness control in [6] are not provably superior.

An artificial viscosity of type (130) is used in all computations, with  $c_1 = 0.5$  and  $c_2 = 1.2$ .

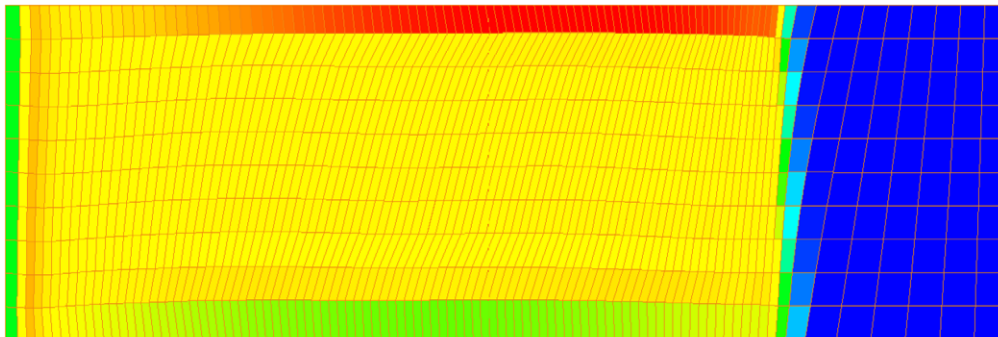
7.3. CFL condition

The following constraint on the time step has been adopted:

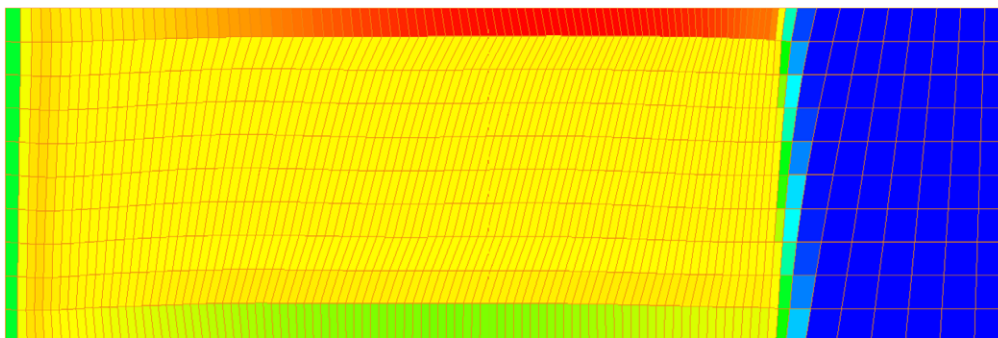
$$\Delta t = \text{CFL} \frac{h_{\min}^2}{v_{\text{tot}} + \sqrt{v_{\text{tot}}^2 + (c_s h_{\min})^2}}, \tag{137}$$



(a) Initial mesh.



(b) Density color plot at  $T = 0.7$ : VMS-I stabilization.



(c) Density color plot at  $T = 0.7$ : FB stabilization.

Fig. 4. Saltzman test: comparison between VMS-I and FB.

where

$$v_{\text{tot}} = v_{\text{art}} + \max(c_s h_e, v_{hg}), \tag{138}$$

and

$$v_{hg} = \begin{cases} \tau \Delta t c_s^2, & \text{for VMS-I,} \\ \tilde{\tau} \Delta t c_s^2, & \text{for VMS-II,} \\ c_{FB} h_e c_s, & \text{for FB,} \end{cases} \tag{139}$$

$$h_{\min} = \min_{1 \leq A \leq n_{\text{np}}} h_A. \tag{140}$$

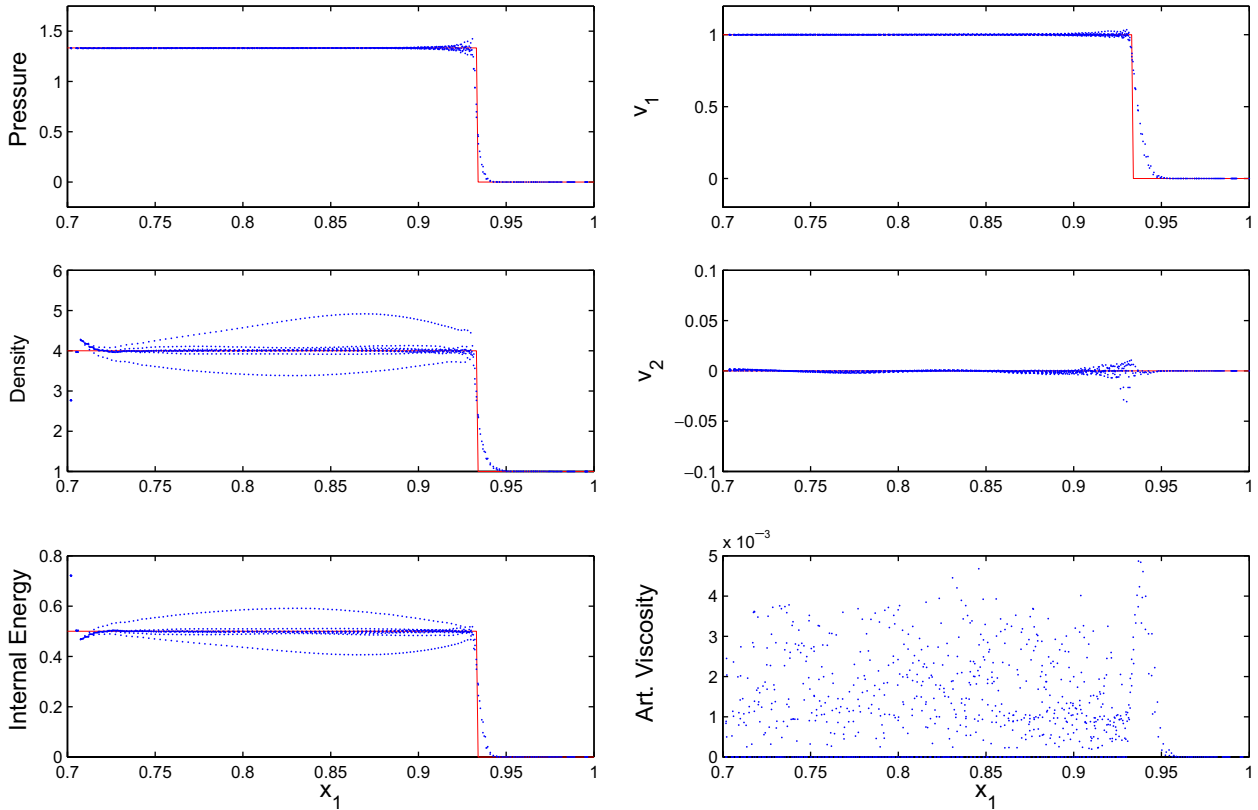


Fig. 5. Saltzman test: The VMS-I approach is compared against the exact solution. The solution is plotted as a function of the coordinate  $x_1$ . On the left column: Pressure, density and internal energy. On the right column: Horizontal velocity  $v_1$ , vertical velocity  $v_2$ , and artificial viscosity  $v_{\text{art}}$ . The exact solution is represented by the continuous line, the dots represent *all* the nodal values of the numerical solution (the  $x_2$ -coordinate locations are projected onto a single plane).

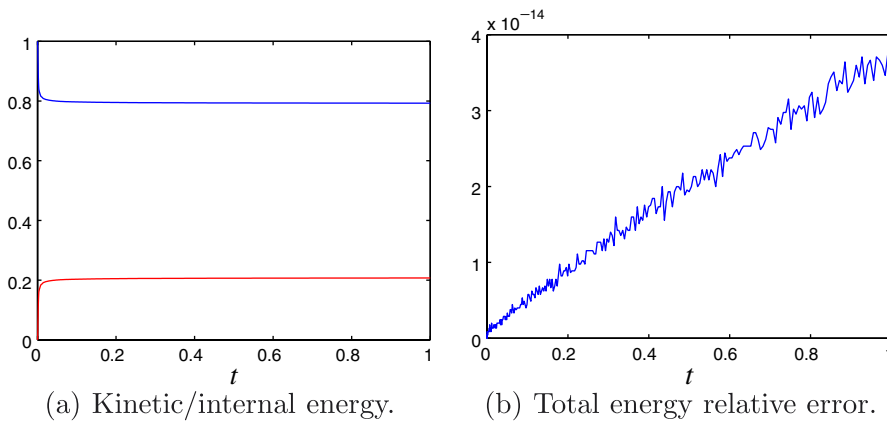


Fig. 6. Energy history for the two-dimensional Sedov test. (a) shows the time history of the kinetic (red) and internal (blue) energies, normalized with respect to the initial total energy,  $\mathcal{E}_0^{\text{tot}}$ . (b) shows the time history of the relative error on the total energy  $(\mathcal{E}^{\text{tot}}(t) - \mathcal{E}_0^{\text{tot}}) / \mathcal{E}_0^{\text{tot}}$ . Notice that the scale of the vertical axis is multiplied by  $10^{-14}$ . (For interpretation of the references in colour in this figure legend, the reader is referred to the web version of this article.)

Here,  $h_{\min}$  is the minimum of the node distances. This definition of the time-step constraint is similar to the one adopted in the LS-DYNA algorithm [15].

**8. Numerical computations in two dimensions**

*8.1. Acoustic pulse computations and hourglass control*

A very interesting test to check the effect of the hourglass control is to propagate an acoustic pulse on a mesh in which the nodes are initially located according to an hourglass pattern (see Fig. 3a). For this specific test, the shock-capturing operator is not applied. The initial conditions are

$$v_0 = \omega, \tag{141}$$

$$\rho_0 = 1 + \omega, \tag{142}$$

$$p_0 = 1 + \omega, \tag{143}$$

$$\omega(X) = \begin{cases} 0.1(1 - \cos((2\pi/\lambda)(X - X_{\text{off}}))), & 0 \leq X - X_{\text{off}} \leq \lambda, \\ 0, & \\ \text{otherwise,} & \end{cases} \tag{144}$$

where  $\lambda$ , the wavelength is taken equal to one fourth of the length the domain  $\Omega_0$ , and  $X_{\text{off}} = -\lambda$ . As time progresses three waves are generated (see Fig. 3b):

- (1) A large amplitude acoustic wave moving from left to right.
- (2) A smaller amplitude acoustic wave moving from right to left.
- (3) A standing (i.e., motionless) entropy wave, characterized by a fluctuation in density and internal energy (not visible in Fig. 3b).

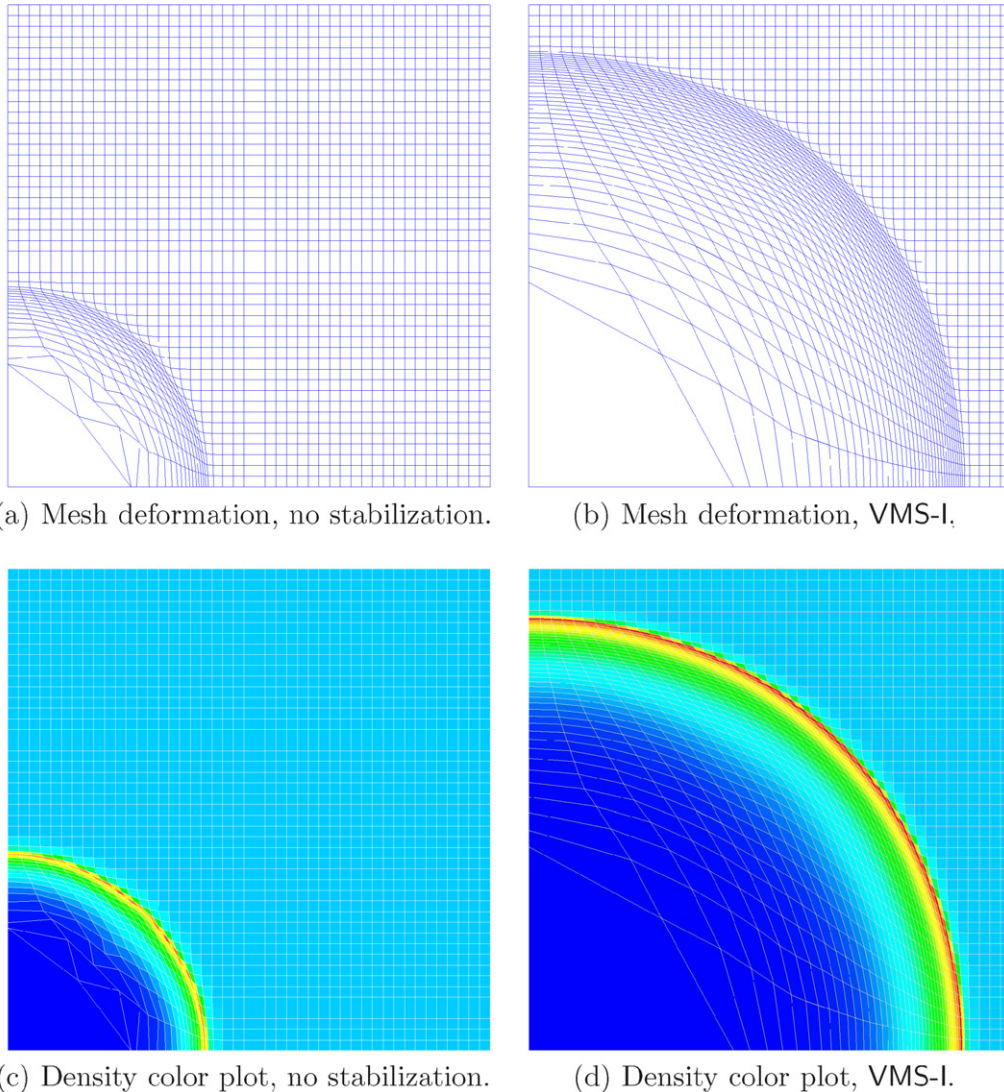
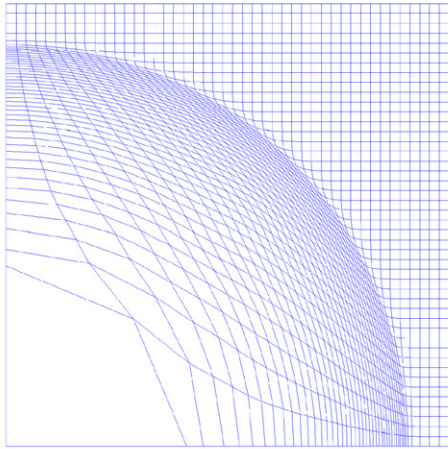
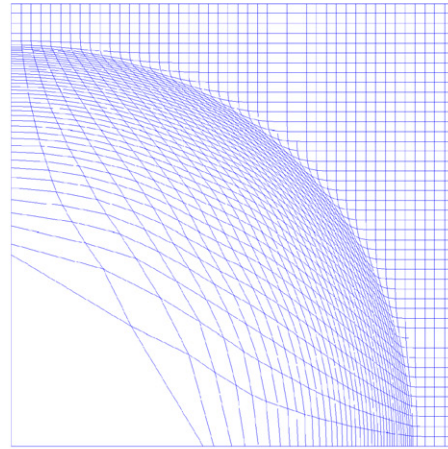


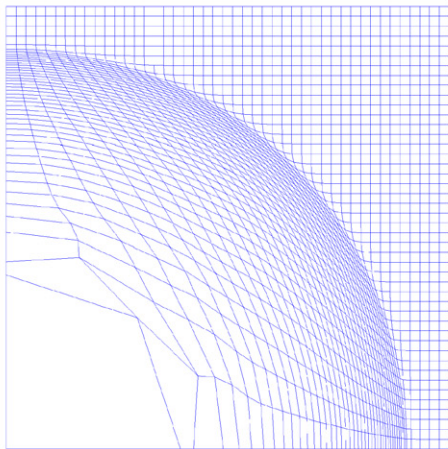
Fig. 7. Two-dimensional Sedov test. Left column: No hourglass stabilization. Right column: VMS-I with full integration of the shock-capturing term. When no stabilization is applied, it is clearly visible a pronounced hourglass pattern, which forces the computation to stop before completion.



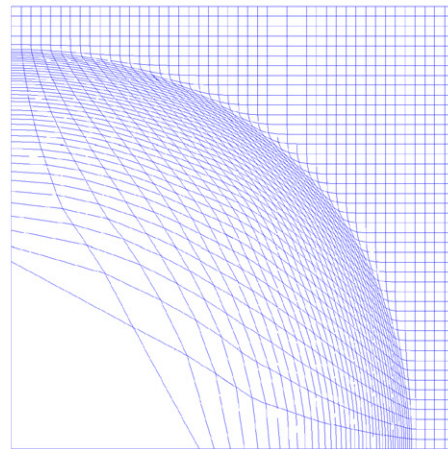
(a) FB, single-point integration quadrature for  $\sigma_{art}$ .



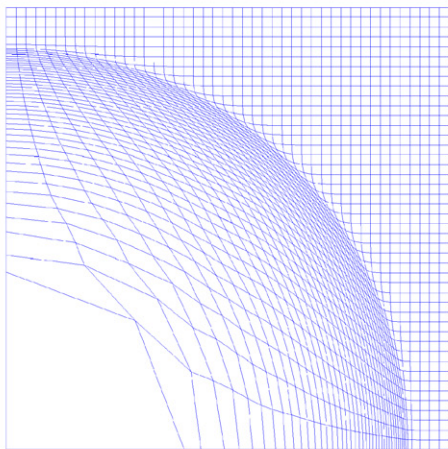
(b) FB, four-point integration quadrature for  $\sigma_{art}$ .



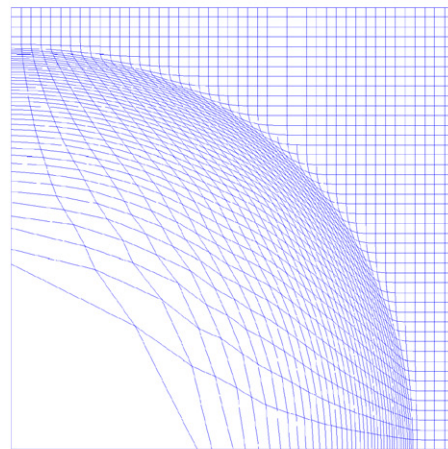
(c) VMS-I, single-point integration quadrature for  $\sigma_{art}$ .



(d) VMS-I, four-point integration quadrature for  $\sigma_{art}$ .



(e) VMS-II, single-point integration quadrature for  $\sigma_{art}$ .



(f) VMS-II, four-point integration quadrature for  $\sigma_{art}$ .

Fig. 8. Two-dimensional Sedov test, comparison of the FB, VMS-I, and VMS-II stabilization approaches. Left column: Single-point integration for  $\sigma_{art}$ . Right column: four-point integration for  $\sigma_{art}$ .

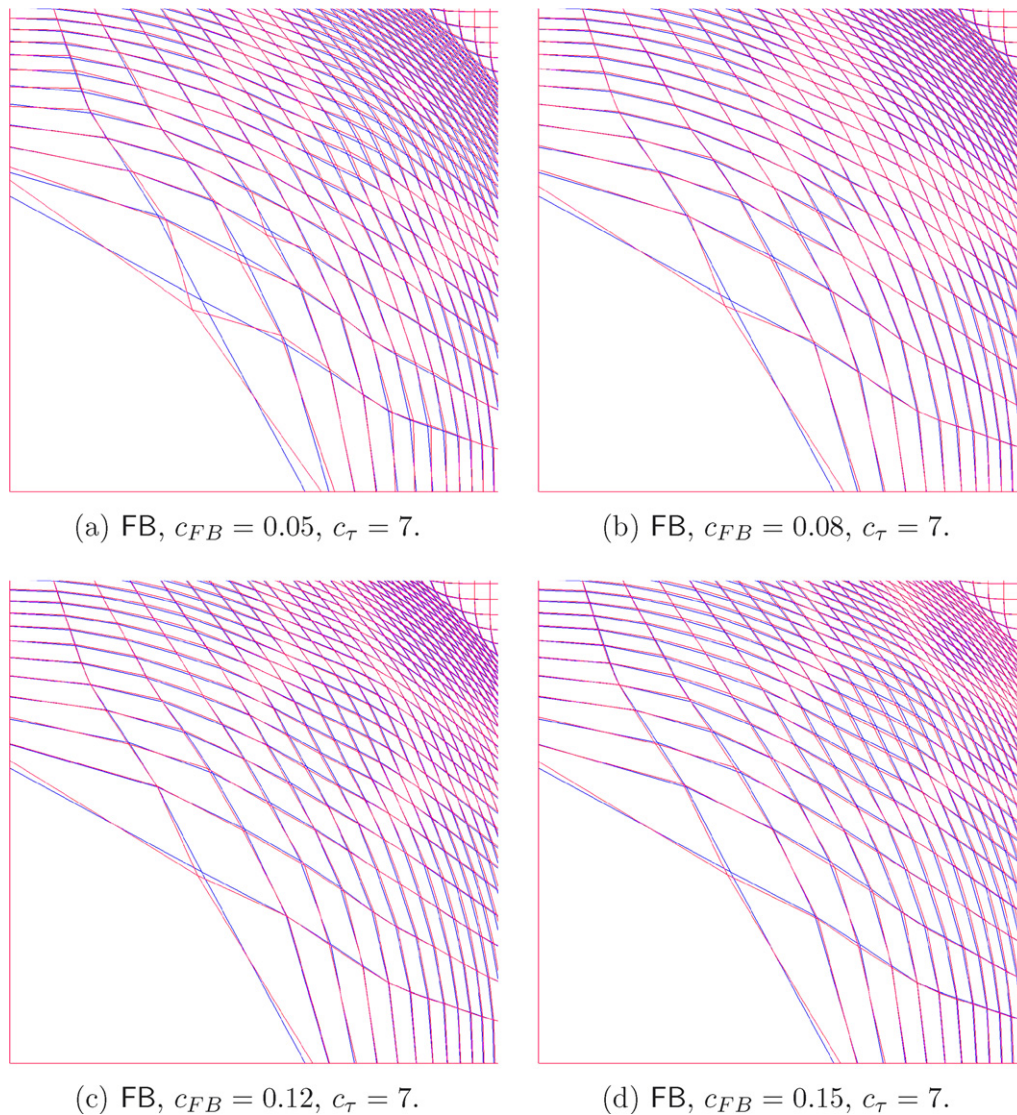


Fig. 9. Two-dimensional Sedov test, zoomed view near the origin. Comparison of the VMS-I and FB stabilization approaches, for different value of the constant parameter in the FB hourglass viscosity. For all four pictures, FB in red, VMS-I in blue. (For interpretation of the references in colour in this figure legend, the reader is referred to the web version of this article.)

It can be seen in Fig. 3c that, when no control is applied, the hourglass modes manifest themselves as oscillations in the velocity. Since the pressure is approximated by piecewise functions which are constant over each element, it is well known that hourglass modes would arise even if multiple-point quadrature were used. This fact was confirmed in computations, not reported here for the sake of brevity. As the VMS-I stabilization is applied (Fig. 3d), the instabilities disappear. For the purposes of comparison, Fig. 3e shows the results for the FB hourglass control. The results of the VMS-I and FB stabilizations are virtually identical.

## 8.2. Saltzman test

The Saltzman test evaluates the ability of a distorted mesh to capture the features of a planar shock. A rectangular domain of gas ( $\gamma = 5/3$ ) is initially at rest.

As it can be seen from the results in Figs. 4b and 5), aside from some over-/under-shoot near the boundaries, the numerical and exact solution show fair agreement. A reason for the over-/under-shoot near the boundaries may be the inaccurate representation of homogeneous gradients in general unstructured meshes for the piecewise constant approximation of the pressure [10]. An analogous result is obtained when the Flanagan–Belytschko hourglass control is applied instead of the multi-scale control (Fig. 4c).

## 8.3. Sedov test

The Sedov test is a multi-dimensional blast test. An exact solution with cylindrical symmetry is derived with self-similarity arguments in [27].

The proposed version of the Sedov blast test is performed on the  $[0,1.1] \times [0,1.1]$  quadrant, subdivided into

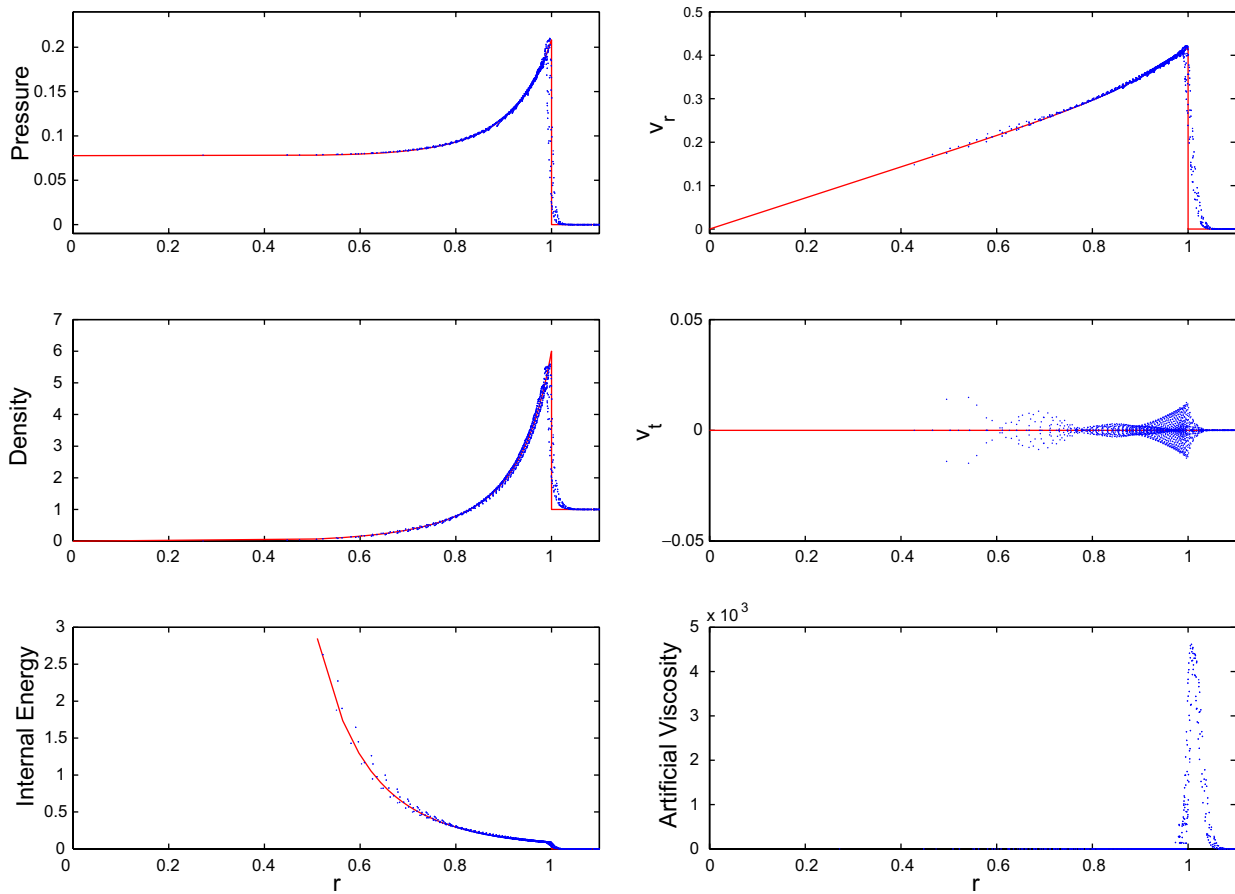


Fig. 10. Two-dimensional Sedov test: Comparison with the exact solution. VMS-I with fully integrated artificial viscosity. On the left column, from the top down: Pressure, density and internal energy. On the right column, from top down: Radial velocity  $v_r$ , tangential velocity  $v_t$ , and artificial viscosity  $v_{\text{art}}$ . Each variable is plotted as a function of the radius  $r = \sqrt{x_1^2 + x_2^2}$ . All solution points are rotated around the origin to align on a single radial plane. Results in the case of single-point integration for the artificial viscosity only, and single-point integration for the entire stress tensor  $\bar{\sigma}$  with Flanagan–Belytschko hourglass control are virtually identical.

45 × 45 squares, and assesses the ability of the method to respect the cylindrical symmetry. The initial mesh configuration, for the sake of brevity, is not shown. The initial density has a uniform unit distribution,  $\gamma = 1.4$ , and the energy is “zero” (actually,  $10^{-14}$ ) everywhere, except the first square zone on the bottom left corner of the quadrant, near the origin, where it takes the value 409.7.

The boundary conditions for the Sedov test, which require vanishing normal components of the velocities, imply that the total energy must be conserved inside the computational domain. Fig. 6a shows the time-history of the total kinetic energy and the total internal energy, normalized with respect to the initial total energy,  $\mathcal{E}_0^{\text{tot}} = \mathcal{E}^{\text{tot}}(t_0)$ . Fig. 6b shows that the relative error in the total energy is on the order of  $10^{-14}$ , confirming that this quantity is conserved throughout the simulation, within the machine precision.

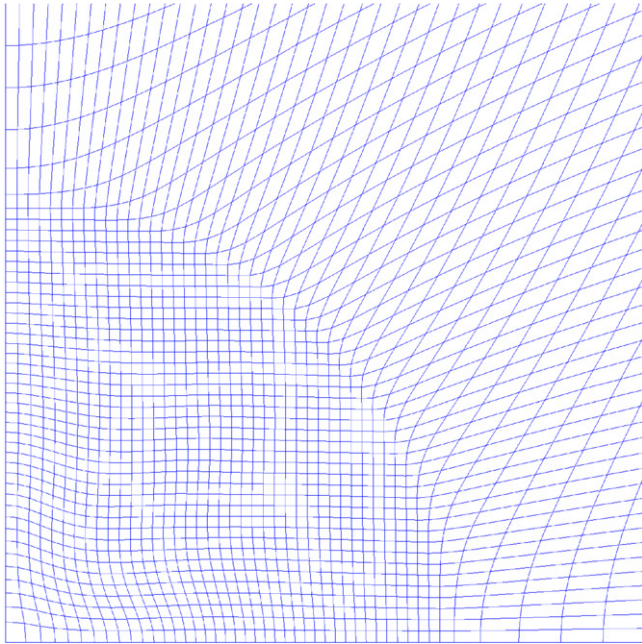
Fig. 7 shows a comparison of the results when no stabilization and VMS-I stabilization are applied. The computation cannot be run to completion, without stabilization, since an hourglass pattern develops (see Fig. 7a). As a consequence, the distance between some of the nodes decreases

progressively during the simulation, forcing the same behavior in the time step, due to the *CFL* constraint. On the contrary, the VMS-I approach runs to completion and with a very smooth mesh and density profiles (Fig. 7b and d). The six pictures composing Fig. 8 show an interesting comparison between the effect of the VMS-I, VMS-II, and FB approaches in combination with different quadrature rules for the artificial viscosity. The effects of non-linear coupling between the artificial viscosity and the VMS-I stabilization term appear clear in Fig. 8c. The best result in terms of smoothness of the final grid configuration and absence of node-to-node oscillations is given by the VMS-I method with full integration of the shock-capturing term (Fig. 8d). If the VMS-I method is combined with single-point integration quadrature, the mesh distortion increases considerably near the origin (Fig. 8c). For single-point integration quadrature, the VMS-II method offers superior results (Fig. 8e).

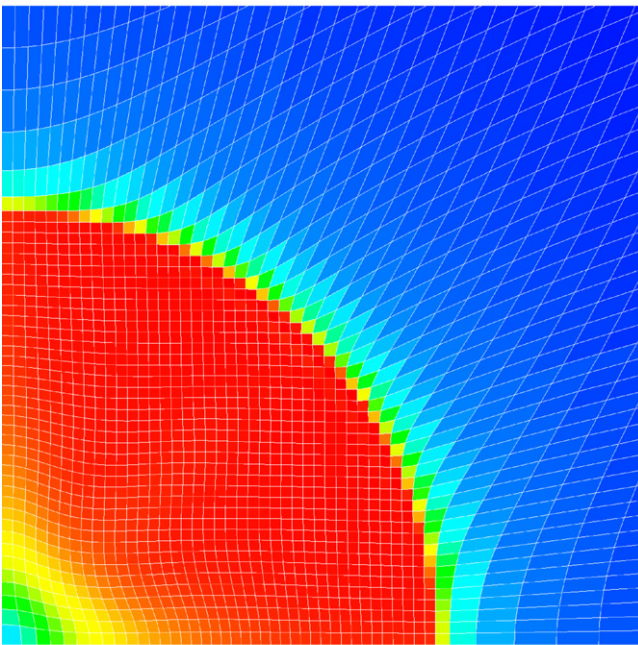
However, when VMS-II is combined with full-quadrature, probably because of the incomplete definition of the pressure residual, the results are less accurate than for the VMS-I method. Fig. 8a and b shows the results for the

FB hourglass control and a constant  $c_{FB} = 0.15$ . The FB yields the best results with single-point integration quadrature integration, but it is somewhat inferior to the VMS-I method when full integration is performed. To see more clearly this last point, Fig. 9 shows a comparison of the VMS-I and the FB approaches, as the constant in the FB viscosity spans the interval  $[0.05, 0.15]$ .

For low values of  $c_{FB}$ , an hourglass pattern, originating in the large element in the lower left corner of the domain,



(a) Mesh deformation.



(b) Density color plot.

Fig. 11. Two-dimensional Noh test on a Cartesian mesh, VMS-I with fully integrated artificial viscosity.

is clearly visible in Fig. 9a. As the constant  $c_{FB}$  is increased (see Fig. 9b–d), the hourglass pattern, although increasingly more damped, persists.

Quantitative comparison between the VMS-I approach and the exact solution to the Sedov problem are shown in Fig. 10: when full integration is applied, the VMS-II and FB yield very similar results. It is worthwhile to notice the peak of the density value at approximately 5.5, against the exact value of 6.0. This is a very accurate result, considering the coarseness of the initial mesh. In the proposed test, perfect cylindrical symmetry is not expected, since, due to the geometry of the mesh and initial/boundary conditions, the geometrical axis of symmetry is the bi-secant of the quadrant. Notice then the perfectly mirrored pattern in the solution for the tangential component of the velocity.

#### 8.4. Noh test

The Noh [22] test is an implosion test. The velocity has an initial uniform radial distribution (the velocity field points to the origin, and has unit magnitude, except at the origin, where it is forced to zero). The initial energy should be zero, but for practical purposes the value  $10^{-14}$  is used. The constant  $\gamma = 5/3$  is applied to all computations. The exact solution for the density behind the shock is 16.0 and decays as  $1 + t/r$  in front of the shock, where  $t$  is time and  $r = \sqrt{x_1^2 + x_2^2}$  is the radius. The pressure past the shock takes the value  $16/3$ . The shock speed is  $1/3$ , so that at the final time of 0.6 in the computation, the discontinuity is found at  $r = 0.2$ .

##### 8.4.1. Noh test on a Cartesian quadrant

Similarly to the case of the Sedov test, a Cartesian quadrant  $[0,1] \times [0,1]$  is initially subdivided into  $50 \times 50$  squares. Mesh deformation and density color plots are presented in Fig. 11: The smoothness of the shocked grid is appreciable. Comparison with the exact solution are presented in Fig. 12. The results show smoothness in all variables, and values of the plateaus for the density and pressure are in good agreement with the exact solution, considering the coarseness of the mesh (for extensive studies on this problem, see, e.g., [22]).

##### 8.4.2. Noh test on a mesh with trisector symmetry

From this variant of the two-dimensional Noh test, very important conclusions can be drawn on some aspects of the artificial viscosity implementation. In particular, this is an interesting test for comparing the performance of  $\sigma_{art}$  as defined in (126) with respect to more classical definition (127). Due to the initial node configuration (see Fig. 13a), the shocked mesh tends to produce homogenous shear modes along the secant lines at  $0^\circ$ ,  $120^\circ$ , and  $240^\circ$ . Shear-induced, “jet-like” patterns can be clearly seen in Fig. 14. The hourglass control is no help in this case, since pure shear motion is pointwise divergence-free, and two-dimensional hourglass modes are not divergence-free. The situation is much improved in the case when the artificial

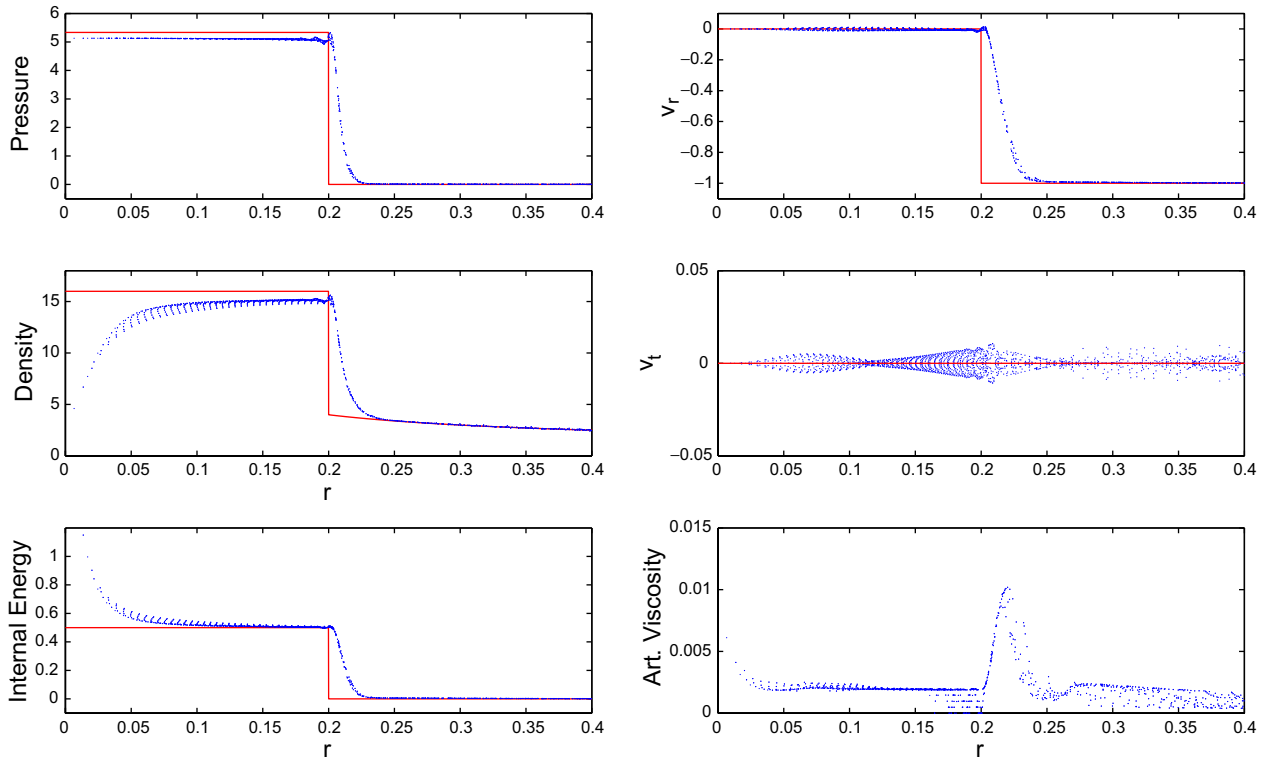
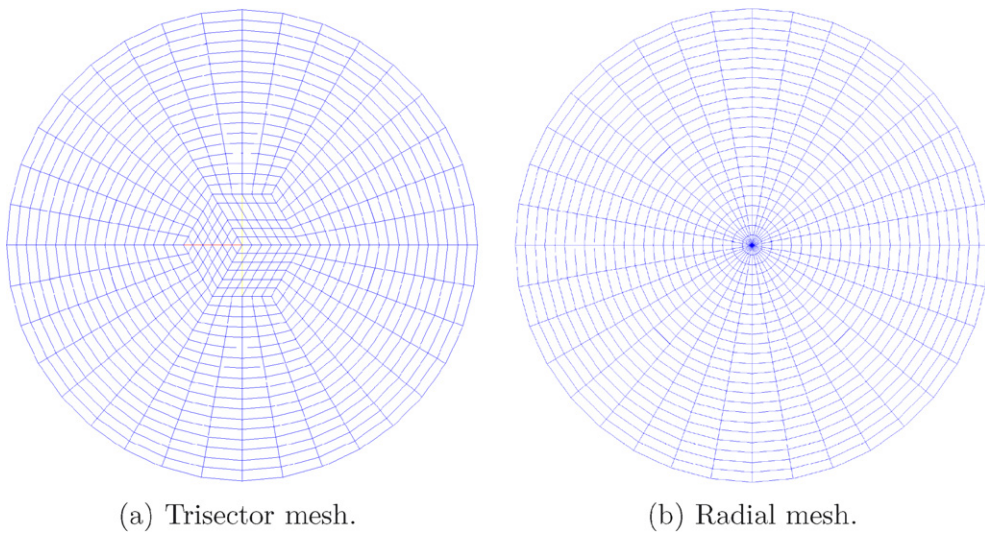


Fig. 12. Two-dimensional Noh test: Comparison with the exact solution. VMS-I with fully integrated artificial viscosity. On the left column, from the top down: Pressure, density and internal energy. On the right column, from top down: Radial velocity  $v_r$ , tangential velocity  $v_t$ , and artificial viscosity  $v_{art}$ . Each variable is plotted as a function of the radius  $r = \sqrt{x_1^2 + x_2^2}$ . All solution points are rotated around the origin to align on a single radial plane.



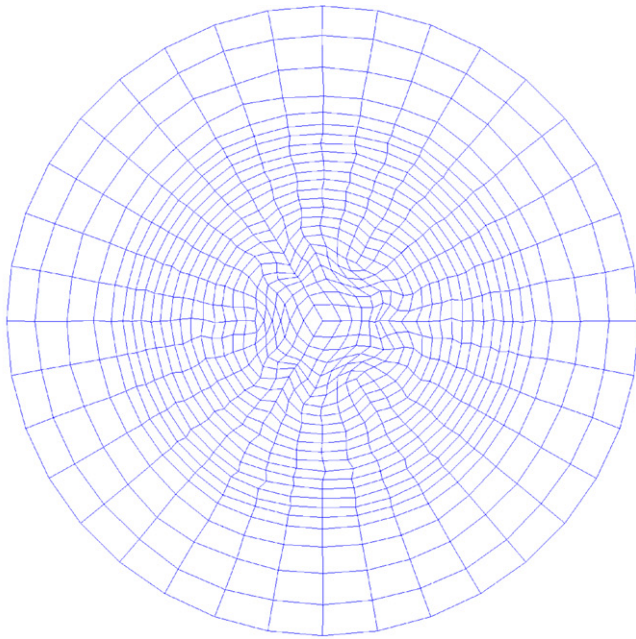
(a) Trisector mesh. (b) Radial mesh.

Fig. 13. Two-dimensional Noh test on a radial trisector mesh. The initial mesh is given by an hexagonal pattern at the center, with a transition to a radially symmetric pattern towards the outside boundary, as shown in (a). The mesh is composed of three identical sectors, rotated by  $120^\circ$  and  $240^\circ$  with respect to one another. (b) presents a radially symmetric mesh, composed of 36 elements along the circumference, and 24 along the radius, which is used to generate a reference solution.

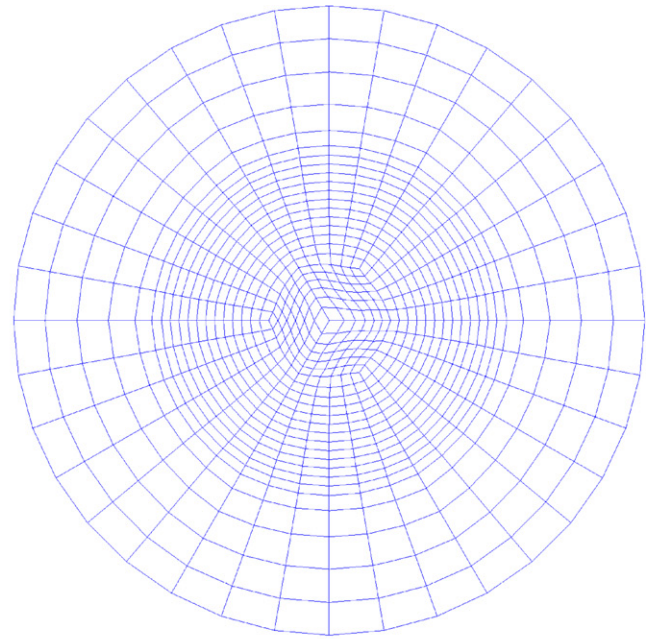
stress  $\sigma_{art}$  is defined according to (126). As can be seen in Fig. 15, shear motion is appropriately damped in the shock layer, and does not propagate to the rest of the flow. Consequently, mesh smoothness, and the accuracy of the solution are much improved (see Fig. 16).

9. Summary

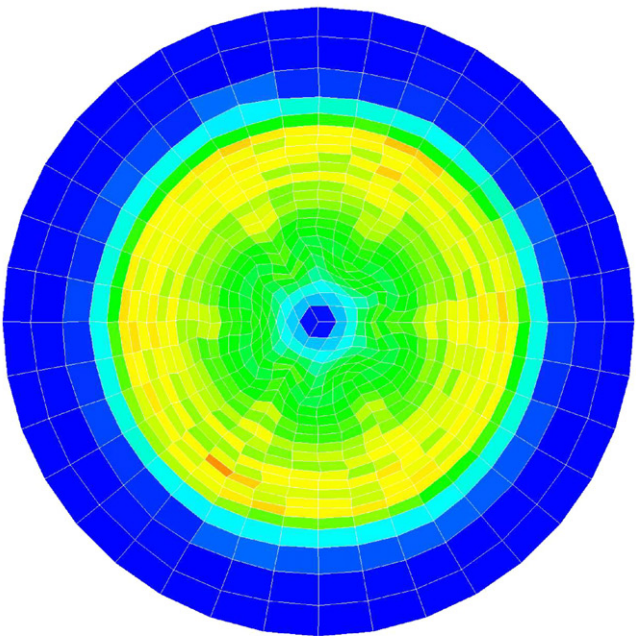
A new multi-scale method for Lagrangian shock hydrodynamics has been presented. The formulation of the proposed method in the context of Q1/P0 finite elements



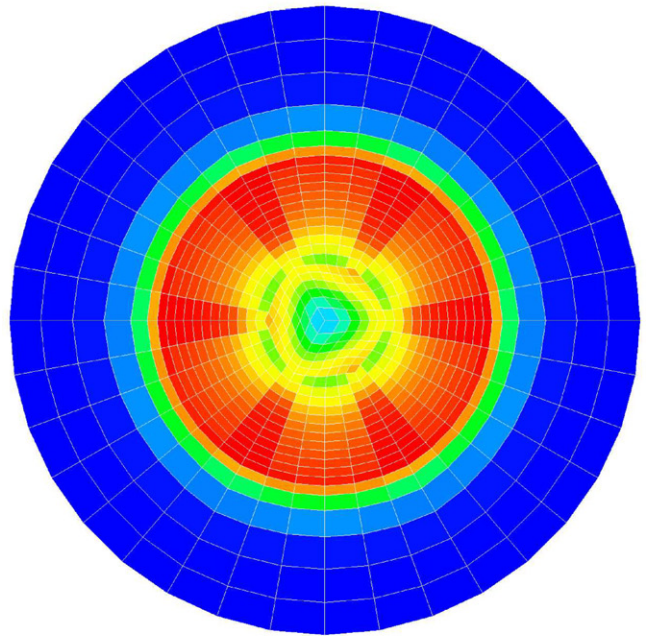
(a) Mesh deformation.



(a) Mesh deformation.



(b) Density color plot.



(b) Density color plot.

Fig. 14. Two-dimensional Noh test on the trisector mesh. FB with the artificial stress tensor  $\sigma_{art}$  defined as in (127).

Fig. 15. Two-dimensional Noh test on the trisector mesh. VMS-I with the artificial stress tensor  $\sigma_{art}$  is defined as in (126). Very similar results are obtained with FB: (a) Mesh deformation and (b) density color plot.

makes it widely applicable to state-of-the-practice hydrodynamic algorithms. The proposed method builds on a mid-point time integrator implemented as a conservative predictor/multi-corrector scheme.

The stabilization augments the original Galerkin formulation without perturbing its global conservation properties. The multi-scale approach leads to a consistent method, in which instabilities (typically, of hourglass type) are controlled by the stabilizing effect of an appropriate

pressure residual. By rational thermodynamic arguments, it has been shown that the pressure residual is tied to the Clausius–Duhem inequality, and effectively, measures the creation of entropy due to instabilities in the numerical discretization. These arguments imply the physical consistency of the multi-scale stabilization. Connections with previous work on physical hourglass stabilization have been drawn. However, the proposed approach takes the

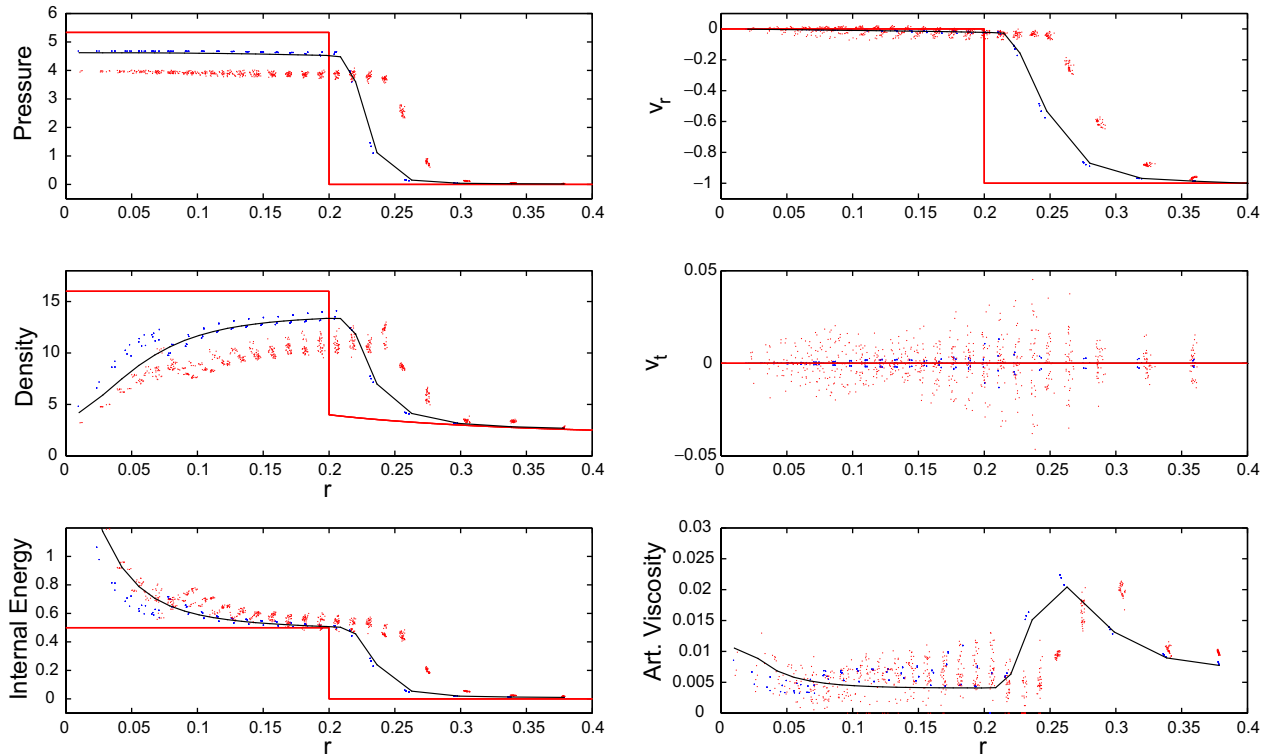


Fig. 16. Two-dimensional Noh test: Comparison with the exact solution (continuous red curve) of the results of Fig. 14 (red dots) and Fig. 15 (blue dots). The continuous black line represents the solution on the radially symmetric mesh of Fig. 13(b), using the tensor artificial viscosity (126). The components of the solution are presented as in Fig. 12. (For interpretation of the references in colour in this figure legend, the reader is referred to the web version of this article.)

discussion to a new level, since, in past developments, many aspects of the interplay between physics and numerics have been overlooked.

Numerical results in two dimensions in the case of compressible gas dynamics show that the method has comparable and in some cases superior performance to state-of-the-practice techniques for hourglass control. In the case of three-dimensional flows, divergence-free, hourglass modes associated with non-homogeneous shear may be present and need stabilization. This fact pinpoints a major disadvantage in fluid computations of the Q1/P0 element, which requires stabilization of fine-scale shear modes, although inviscid fluids have no shear strength or shear damping mechanisms. In particular, the pressure residual cannot detect the divergence-free unstable hourglass modes, and additional stabilization mechanisms acting on the deviator of the velocity gradient are required [26]. In this context, the multi-scale analysis provides a new perspective, and allows for a more flexible design of hourglass viscosities aimed at damping such instabilities. In light of the encouraging exploratory simulations in [26], more work is needed to fully investigate the robustness and accuracy properties of the proposed framework for three-dimensional computations of inviscid fluids.

In the case of solids, instead, the “plain-vanilla” multi-scale approach should incorporate all the necessary stabilization mechanism for Q1/P0 formulations in two and three

space dimensions. This is due to the fact that, for materials with shear strength, the stabilizing residual is given by the stress update equation, which provides the necessary physical mechanisms for the control of the entire space of hourglass modes.

Of great importance are also the extensions of the proposed multi-scale approach to more complex computations, involving multi-material, multi-physics applications.

### Acknowledgements

The research work of G. Scovazzi and E. Love was partially funded by the DOE NNSA Advanced Scientific Computing Program and the Computer Science Research Institute (CSRI) at Sandia National Laboratories. The partial support through LDRD “A Mathematical Framework for Multi-scale Science and Engineering: The Variational Multi-scale Method and Interscale Transfer Operators” is also acknowledged. LDRD funding was essential in the early stage of development, when the outcome of this research was still uncertain. The work of M. Shashkov was carried out under the auspices of the National Nuclear Security Administration of the US Department of Energy at Los Alamos National Laboratory under Contract No. DE-AC52-06NA25396 and has been supported by DOE Office of Science Advanced Computing Research (ASCR) program in Applied Mathematical Sciences.

We would like to thank Professor Thomas J.R. Hughes, and Dr. Pavel Bochev, Dr. Allen Robinson, and Dr. John Shadid for very insightful discussions. Many thanks also to Dr. Greg Weirs for providing us with very insightful test cases. The first two authors would like to thank Dr. Randy Summers, Dr. John Shadid, Dr. Allen Robinson, and Dr. Scott Collis for their genuine support.

## References

- [1] S.S. Antman, *Nonlinear problems of elasticity*, Applied Mathematical Sciences, Second ed., vol. 107, Springer, New York, 2005.
- [2] A. Barlow, A compatible finite element multi-material ALE hydrodynamics algorithm, *Int. J. Numer. Methods Fluids*, in press, doi:10.1002/fld.1593.
- [3] T. Belytschko, L.P. Bindeman, Assumed strain stabilization of the 4-node quadrilateral with 1-point quadrature for nonlinear problems, *Comput. Methods Appl. Mech. Engrg.* 88 (3) (1991) 311–340.
- [4] T. Belytschko, L.P. Bindeman, Assumed strain stabilization of the eight node hexahedral element, *Comput. Methods Appl. Mech. Engrg.* 105 (2) (1993) 225–260.
- [5] T. Belytschko, W.K. Liu, B. Moran, *Nonlinear Finite Elements for Continua and Structures*, J. Wiley & Sons, New York, 2000.
- [6] D.J. Benson, A new two-dimensional flux-limited shock viscosity for impact calculations, *Comput. Methods Appl. Mech. Engrg.* 93 (1991) 39–95.
- [7] D.J. Benson, Computational methods in Lagrangian and Eulerian hydrocodes, *Comput. Methods Appl. Mech. Engrg.* 99 (1992) 235–394.
- [8] E.J. Caramana, D.E. Burton, M.J. Shashkov, P.P. Whalen, The construction of compatible hydrodynamics algorithms utilizing conservation of total energy, *J. Comput. Phys.* 146 (1998) 227–262.
- [9] D.E. Carlson, Linear thermoelasticity, in: C.A. Truesdell (Ed.), *Mechanics of Solids*, vol. II, Springer-Verlag, New York, 1984, pp. 297–345 (Chapter 2).
- [10] M.A. Christon, Pressure gradient approximations for staggered-grid finite element hydrodynamics, *Int. J. Numer. Methods Fluids*, 2007, in preparation.
- [11] R. Codina, J. Principe, O. Guasch, S. Badia, Time dependent subscales in the stabilized finite element approximation of incompressible flow problems, *Comput. Methods Appl. Mech. Engrg.* 196 (21–24) (2007) 2413–2430.
- [12] B.D. Coleman, V.J. Mizel, Existence of caloric equations of state in thermodynamics, *J. Chem. Phys.* 40 (4) (1964) 1116–1125.
- [13] D.P. Flanagan, T. Belytschko, A uniform strain hexahedron and quadrilateral with orthogonal hourglass control, *Int. J. Numer. Methods Engrg.* 17 (5) (1981) 679–706.
- [14] G.L. Goudreau, J.O. Hallquist, Recent developments in large-scale finite element Lagrangian hydrocode technology, *Comput. Methods Appl. Mech. Engrg.* 33 (1–3) (1982) 725–757.
- [15] J.O. Hallquist, LS-DYNA theory manual, Technical report, Livermore Software Technology Corporation, Livermore, CA, March 2006, <http://www.lstc.com>.
- [16] T.J.R. Hughes, *The Finite Element Method: Linear Static and Dynamic Finite Element Analysis*, Prentice-Hall, Englewood Cliffs, New Jersey, 1987 (Dover reprint, 2000).
- [17] T.J.R. Hughes, Multiscale phenomena: Green’s functions, the Dirichlet-to-Neumann formulation, subgrid-scale models, bubbles and the origin of stabilized methods, *Comput. Methods Appl. Mech. Engrg.* 127 (1995) 387–401.
- [18] T.J.R. Hughes, G.R. Feijóo, L. Mazzei, J.-B. Quincy, The Variational Multiscale Method—a paradigm for computational mechanics, *Comput. Methods Appl. Mech. Engrg.* 166 (1998) 3–24.
- [19] T.J.R. Hughes, M. Mallet, A. Mizukami, A new finite element formulation for computational fluid dynamics: II. Beyond SUPG, *Comput. Methods Appl. Mech. Engrg.* 54 (1986) 341–355.
- [20] T.J.R. Hughes, G. Scovazzi, L.P. Franca, Multiscale and stabilized methods, in: E. Stein, R. de Borst, T.J.R. Hughes (Eds.), *Encyclopedia of Computational Mechanics*, John Wiley & Sons, 2004.
- [21] V.F. Kuropatenko, On difference methods for the equations of hydrodynamics, in: N.N. Janenko (Ed.), *Difference Methods for Solutions of Problems of Mathematical Physics, I*, American Mathematical Society, Providence, RI, 1967.
- [22] W.F. Noh, Errors for calculations of strong shocks using an artificial viscosity and an artificial heat flux, *J. Comput. Phys.* 72 (1987) 78–120.
- [23] M.A. Puso, A highly efficient enhanced assumed strain physically stabilized hexahedral element, *Int. J. Numer. Methods Engrg.* 49 (8) (2000) 1029–1064.
- [24] G. Scovazzi, Stabilized shock hydrodynamics: II. Design and physical interpretation of the SUPG operator for Lagrangian computations, *Comput. Methods Appl. Mech. Engrg.* 196 (4–6) (2007) 966–978.
- [25] G. Scovazzi, M.A. Christon, T.J.R. Hughes, J.N. Shadid, Stabilized shock hydrodynamics: I. A Lagrangian method, *Comput. Methods Appl. Mech. Engrg.* 196 (4–6) (2007) 923–966.
- [26] G. Scovazzi, E. Love, M.J. Shashkov, A multi-scale Q1/P0 approach to Lagrangian shock hydrodynamics, Technical report, SAND2007-1423, Sandia National Laboratories, New Mexico, March 2007, <http://www.cs.sandia.gov/~gscovaz>.
- [27] L.I. Sedov, *Similarity and Dimensional Methods in Mechanics*, Academic Press, New York, 1959.
- [28] J.C. Simo, T.J.R. Hughes, *Computational Inelasticity*, Springer, New York, 1998.
- [29] J.C. Simo, N. Tarnow, The discrete energy-momentum method. Conserving algorithms for nonlinear elastodynamics, *Z. Angew. Math. Phys. (ZAMP)* 43 (5) (1992) 757–792.
- [30] T.E. Tezduyar, M. Senga, Stabilization and shock-capturing parameters in SUPG formulation of compressible flows, *Comput. Methods Appl. Mech. Engrg.* 195 (2006) 1621–1632.
- [31] C.A. Truesdell, *Rational Thermodynamics*, Second ed., Springer-Verlag, New York, 1984.
- [32] C.A. Truesdell, W. Noll, *The non-linear field theories of mechanics*, Second ed., Springer-Verlag, New York, 1992.
- [33] F. Van der Ween, T. Belytschko, Correction of article by D.P. Flanagan and T. Belytschko, *Int. J. Numer. Methods Engrg.* 19 (3) (1983) 467–468.